CHCHD10S59L/+ mouse model: Behavioral and neuropathological features of frontotemporal dementia

Emmanuelle C Genin, Pauline Pozzo Di Borgo, Thomas Lorivel, Sandrine Hugues, Mélissa Farinelli, Alessandra Mauri-Crouzet, Françoise Lespinasse, Lucas Godin, Véronique Paquis-Flucklinger, Agnès Petit-Paitel

▶ **To cite this version:**

Emmanuelle C Genin, Pauline Pozzo Di Borgo, Thomas Lorivel, Sandrine Hugues, Mélissa Farinelli, et al.. CHCHD10S59L/+ mouse model: Behavioral and neuropathological features of frontotemporal dementia. Neurobiology of Disease, 2024, 195, pp.106498. 10.1016/j.nbd.2024.106498 . hal-04774507

HAL Id: hal-04774507
https://hal.science/hal-04774507v1

Submitted on 8 Nov 2024

HAL is a multi-disciplinary open access archive for the deposit and dissemination of scientific research documents, whether they are published or not. The documents may come from teaching and research institutions in France or abroad, or from public or private research centers.

L'archive ouverte pluridisciplinaire **HAL**, est destinée au dépôt et à la diffusion de documents scientifiques de niveau recherche, publiés ou non, émanant des établissements d'enseignement et de recherche français ou étrangers, des laboratoires publics ou privés.

Neurobiology of Disease 195 (2024) 106498

Contents lists available at ScienceDirect

Neurobiology of Disease

journal homepage: www.elsevier.com/locate/ynbdi

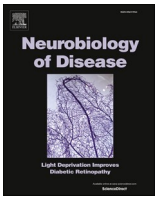

CHCHD10$^{S59L/+}$ mouse model: Behavioral and neuropathological features of frontotemporal dementia

Emmanuelle C. Genin [a,1], Pauline Pozzo di Borgo [b,1], Thomas Lorivel [b], Sandrine Hugues [c], Mélissa Farinelli [c], Alessandra Mauri-Crouzet [a], Françoise Lespinasse [a], Lucas Godin [b], Véronique Paquis-Flucklinger [a,**,2], Agnès Petit-Paitel [b,2,*]

[a] Université Côte d'Azur (UniCa), Institute for Research on Cancer and Aging (IRCAN), UMR CNRS 7284/INSERM U1081, Centre Hospitalier Universitaire (CHU) de Nice, Nice, France
[b] Université Côte d'Azur (UniCa), Institut de Pharmacologie Moléculaire et Cellulaire (IPMC), CNRS UMR7275, Inserm, Sophia Antipolis, Valbonne, France
[c] E-Phy-Science, Bioparc, 2400 Route des Colles, Sophia Antipolis 06410, Biot, France

ARTICLE INFO

Keywords:
CHCHD10
Mitochondrion
Frontotemporal dementia
Amyotrophic lateral sclerosis
Mouse model

ABSTRACT

CHCHD10-related disease causes a spectrum of clinical presentations including mitochondrial myopathy, cardiomyopathy, amyotrophic lateral sclerosis (ALS) and frontotemporal dementia (FTD). We generated a knock-in mouse model bearing the p.Ser59Leu (S59L) *CHCHD10* variant. *Chchd10*$^{S59L/+}$ mice have been shown to phenotypically replicate the disorders observed in patients: myopathy with mtDNA instability, cardiomyopathy and typical ALS features (protein aggregation, neuromuscular junction degeneration and spinal motor neuron loss). Here, we conducted a comprehensive behavioral, electrophysiological and neuropathological assessment of *Chchd10*$^{S59L/+}$ mice. These animals show impaired learning and memory capacities with reduced long-term potentiation (LTP) measured at the Perforant Pathway-Dentate Gyrus (PP-DG) synapses. In the hippocampus of *Chchd10*$^{S59L/+}$ mice, neuropathological studies show the involvement of protein aggregates, activation of the integrated stress response (ISR) and neuroinflammation in the degenerative process. These findings contribute to decipher mechanisms associated with *CHCHD10* variants linking mitochondrial dysfunction and neuronal death. They also validate the *Chchd10*$^{S59L/+}$ mice as a relevant model for FTD, which can be used for preclinical studies to test new therapeutic strategies for this devastating disease.

1. Introduction

Frontotemporal dementia (FTD) represents one of the most common form of dementia in people under 65 years of age (Ratnavalli et al., 2002). This disease is characterized by changes in behavior and/or language due to the relatively selective atrophy of the frontal and temporal lobes of the brain (For review see (Snowden, 2023)). FTD overlaps with amyotrophic lateral sclerosis (ALS), a motor neuron disease (MND) leading to a defect of the neuromuscular system and death from respiratory failure 2 to 3 years after the onset of symptoms. FTD

Abbreviations: Iba1, Actin-binding protein; ALS, Amyotrophic Lateral Sclerosis; BAM, CNS-Border-Associated Macrophage; BBB, Blood-Brain Barrier; CA, *Cornus Ammonis*; CHCHD10, Coiled-Coil-Helix-Coiled-Coil-Helix Domain Containing protein 10; CHMP2B, Charged Multivesicular Body Protein 2B; CMT2, Charcot-Marie-Tooth disease type 2; CNS, Central Nervous System; C9orf72, Chromosome 9 open reading frame 72; DG, Dentate Gyrus; eIF2, eukaryotic translation initiation factor 2; FTD, Frontotemporal Dementia; HFS, High Frequency Stimulation; IMM, inner mitochondrial membrane; KI, knock-in; LTP, Long Term Potentiation; MN, motor neuron; MND, motor neuron disease; mtISR, mitochondrial integrated stress response; NMJ, neuromuscular junction; NORT, Novel Object Recognition Test; PVM, Peri Vascular Macrophage; PTP, Post-Tetanic Potentiation; VCP, Valosin Containing Protein; PHB, Prohibitin; RC, respiratory chain; SLP2, Stomatin-Like Protein 2; SMAJ, late-onset spinal motor neuropathy; SQSTMI, Sequestosome 1; TARDBP, TAR DNA Binding Protein; UBQLN2, Ubiquilin 2; WT, wild-type..

* Correspondence to: Agnès Petit-Paitel, IPMC, CNRS UMR7275, INSERM U1323, 660 Route des Lucioles, Sophia Antipolis, Valbonne 06560, France.
** Correspondence to: Véronique Paquis-Flucklinger, IRCAN, UMR CNRS 7284/INSERM U1081, Medicine School, 28 av de Valombrose, Nice, cedex 2 06107, France.
E-mail addresses: paquis@unice.fr (V. Paquis-Flucklinger), paitel@ipmc.cnrs.fr (A. Petit-Paitel).
[1] These authors contributed equally to this work.
[2] These authors are co-last and co-corresponding authors.

https://doi.org/10.1016/j.nbd.2024.106498
Received 25 January 2024; Received in revised form 22 March 2024; Accepted 4 April 2024
Available online 5 April 2024
0969-9961/© 2024 The Authors. Published by Elsevier Inc. This is an open access article under the CC BY-NC license (http://creativecommons.org/licenses/by-nc/4.0/).

and ALS share a same clinical spectrum with 50% of ALS patients showing frontal lobe dysfunction and 15% of FTD patients developing ALS features. FTD and ALS also overlap genetically with several genes, like *C9orf72*, *TARDBP, VCP*, *SQSTMI*, *UBQLN2*, *CHMP2B or CHCHD10,* involved in both diseases (For review see (Parobkova and Matej, 2021)). Mouse models are very important for understanding these pathologies and for preclinical studies to test candidate molecules *in vivo*. With the increasing identification of the number of genes involved in the ALS-FTD spectrum, numerous mouse models have been described in recent years (for review see Ahmed et al., 2017). A large number of these models correspond to transgenic animals leading to expression level much higher than the one of the endogenous gene (TDP-43, tau, VCP…). Given that most of the proteins involved will be found as aggregates, it is preferable to work with endogenous expression levels. KI models expressing mutations identified in patients are to be preferred. However, variants that are deleterious in human do not necessarily lead to pathology in mouse. In the end, KI models that recapitulate the signs observed in patients with behavioral changes and memory dysfunction are currently rare.

Mitochondria are eukaryotic organelles that act as metabolic hubs and signaling platforms that are of central importance in every tissue of the body. Mitochondrial diseases, characterized by a respiratory chain (RC) deficiency, display heterogeneous clinical presentations in terms of age at onset, progression and symptoms. Interestingly, we identified a heterozygous variant (p.Ser59Leu, S59L) in the gene encoding the mitochondrial Coiled-Coil-Helix-Coiled-Coil-Helix Domain Containing protein 10 (CHCHD10) in two families. In the first one, patients developed a late-onset mitochondrial myopathy and other symptoms including MND, cognitive decline resembling FTD and cerebellar ataxia (Bannwarth et al., 2014) (Chaussenot et al., 2014). In the second family, the same S59L variant was responsible for a typical ALS-FTD. In both families, the transmission of the disease was autosomal dominant. Since then, the spectrum of *CHCHD10*-related diseases has broadened considerably (for review see (Genin et al., 2023)), including early-onset mitochondrial myopathies (Ajroud-Driss et al., 2015), cardiomyopathies (Shammas et al., 2022), ALS (Johnson et al., 2014), FTD (Sirkis et al., 2019), late-onset spinal motor neuropathy (SMAJ) (Penttilä et al., 2015) (Müller et al., 2014), and Charcot-Marie-Tooth disease type 2 (CMT2) (Auranen et al., 2015).

The precise function of CHCHD10 in mitochondria is unclear. Fibroblasts from patients carrying the S59L mutation ($CHCHD10^{S59L/+}$) display RC deficiency, mitochondrial ultrastructural alterations with loss of cristae, and fragmentation of the mitochondrial network (Bannwarth et al., 2014) (Genin et al., 2016). The analysis of these cells provided us with important information (Genin et al., 2018), however, specific neuronal models needed to understand the biological function of CHCHD10 and the impact of pathogenic mutations were lacking. We generated whole-body knock-in (KI) mice carrying the S59L point mutation (Genin et al., 2019). $Chchd10^{S59L/+}$ mice appeared normal at birth but fail to gain weight normally beginning at 10 weeks of age. Around one year old, they presented the mitochondrial myopathy observed in the patients from our original family. Their condition worsened rapidly with severe weight loss and tremors and they developed a severe mitochondrial cardiomyopathy, leading to the death of the animals before 14 months of age. At the end-stage of the disease, $Chchd10^{S59L/+}$ animals displayed typical signs of MND including neuromuscular junction (NMJ) and motor neuron (MN) degeneration with significant MN loss in the spinal cord. We also observed TDP-43 cytoplasmic aggregates in spinal neurons, corresponding to the TDP-43 proteinopathy found in ALS patients (Genin et al., 2019).

In this study, we show that $Chchd10^{S59L/+}$ mice display typical FTD features including impairment of learning and memory abilities with protein aggregates, increased neuronal death and inflammatory activation of microglia and astrocytes in the hippocampus and parahippocampal regions. These results show that $Chchd10^{S59L/+}$ mice are also a relevant model for FTD.

2. Materials and methods

2.1. $Chchd10^{S59L/+}$ mice

All animal procedures were approved by the Ministère de l'Education Nationale, de l'Enseignement Supérieur et de la Recherche (MESR agreements: APAFIS#5870–2,016,061,017,306,888 and APAFIS#2285 1–2,019,110,715,009,566). $Chchd10^{S59L/+}$ mice were generated in a previous work (Genin et al., 2019). They were housed at the IPMC and IRCAN facilities with a 12 h light/12 h dark cycle and allowed food and water *ad libitum*. For behavioral studies, male and female mice were acclimatized to the test room for 30 to 45 min before the start of training or testing. For electrophysiology analysis, all animal experiments were conducted in accordance with *E*-PHY-SCIENCE's bioethical guidelines, which are fully compliant to internationally accepted principles for the care and use of laboratory animals (APAFIS#35798–2,022, 030,115,349,107).

2.2. Grip strength

The maximal muscle strength of forelimbs was measured using a digital grip-strength meter (Bioseb, Vitrolles, France). The apparatus consisted of a grid of stainless-steel rods (2 mm in diameter) connected to a force transducer. At the beginning of each trial, the experimenter held the mice by the base of the tail, allowing the animals to grasp one of the rods with their forepaws. As soon as the mice grasped it, they were gently and progressively pulled backwards by the tail until the grip was lost. The peak force was automatically recorded in grams (g) by the device. The testing phase consisted of recording 3 trials for each mouse, which were then averaged.

2.3. Rotarod

Motor coordination and balance were measured by Rotarod (Ugo-Basile, Gemonio, Italy). Mice were placed on a rotating rod for two habituation sessions (5 min each) at constant speed (4 rpm/min), 4 h apart. For the testing phase, mice were placed on a rotating rod set to accelerate from 4 to 40 rpm in 300 s. Trial began when acceleration was started and ended when animal fell off rod. The procedure was repeated three times a day for 2 days (48 h apart, Inter Trial Interval = 2 h).

2.4. Parallel rod floor

The parallel rod floor test allowed the simultaneous measurement of ataxia and locomotor activity. This test evaluated the ability of the mice to accurately place the front paws or hind paws during spontaneous exploration of an elevated grid. In brief, mice were placed in a 20 × 20 × 28.5 cm^3 acrylic chamber with a wire grid (stainless-steel rods of 1.6 mm in diameter) as a raised floor (Stoelting Europe, Dublin, Ireland). Mice were allowed to freely move for 300 s. The distance crossed and the number of foot slip errors were recorded over a period of 5 min. The number of slips per minute of walking was then calculated.

2.5. Pole test

The pole test was used to assess basal ganglia related movement disorders in mice. The procedure evaluated the ability of a mouse to grasp and maneuver on a pole back to the bottom. Mice were placed with their head oriented upward on top of a rough-surfaced pole (8 mm in diameter and 50 cm in height). The time required for the animals to orient themselves facing in a downward direction (time to turn) and to descend to the base of the pole (total time) was recorded for three trials.

2.6. Actimetry

Spontaneous locomotor activity and rearings were measured using

an actimeter apparatus (Imetronic, Marcheprime, France). Briefly, the mice were left for 3 days in individual cages (20.5 × 11.5 × 16.5 cm^3) equipped with infrared beams able to detect horizontal and vertical movements. At the start of experiment, the cages were placed in an enclosure under 12 h light/dark cycle (lights on at 8:00 AM). The variables collected were: number of rearings, front activity, back activity, and locomotion.

2.7. Elevated Plus Maze

The Elevated Plus Maze test was used to assess anxiety-related behavior in our mice. The apparatus (Intellibio, Seichamps, France) was made of plastic material and consisted of two open (30 × 5 × 15 cm^3) and closed (30 × 5 × 15 cm^3) arms connected to a central area (5 × 5 cm), with the arms of the same type facing each other. The open arms were surrounded by a 1-mm-high ledge to prevent the mice from falling. The whole apparatus was elevated to a height of 50 cm above floor level. The illumination was set at 100 lx. At the beginning of the test, mice were individually placed at the center facing an open arm, and their behavior was video recorded for 5 min. The number of entries and the time spent in the open and closed arms were analyzed using the ANY-Maze video tracking system (Stoelting Europe, Dublin, Ireland). The percentage of entries and time spent in the open arms relative to the total entries and time spent in the four arms, which are classical indices of anxiety, were calculated *a posteriori*.

2.8. Barnes maze

The Barnes maze was designed for testing spatial learning and memory. Mice were placed in the middle of a circular platform with 20 equally spaced holes (5 cm in diameter) around the perimeter. One of these holes was connected to a dark escape chamber called target box. Bright light (450 lx) shed on the platform was used to encourage mice to find it by spatial navigation using extra-maze visual cues placed on the walls of the testing room. Mice had a period of habituation, during which they were able to freely explore the device, without the target box, for 2 min. One day after, they started a spatial acquisition phase that lasted for 4 days with 3 trials per day and 45 min between each trial. At the beginning of each trial, mice were placed in the center of the maze under a rectangular opaque box. The box was then removed and mice were allowed to explore the maze. The trial ended when mice entered the escape box or after 3 min. In this case, mice were gently guided to the escape box by the experimenter and remained there for 1 min. On day 1 and day 8 after the training sessions, mice went through the reference memory phases, during which the target box was removed and the mouse was left free to explore for 90 s. The latency to find the target box during each trial as well as the number of visits to each hole during the memory phases were recorded with the assistance of ANY-Maze video tracking system (Stoelting Europe, Dublin, Ireland). The cumulated number of visits to the target hole and to the two holes on both sides of the latter were then calculated as an additional index of spatial navigation precision.

2.9. Open-field and novel object recognition test

The open-field was used to assess exploratory- and anxiety-related behaviors. The novel object recognition test was used to assess recognition memory. On two consecutive days, mice were familiarized with an open-field (40 × 40 × 30 cm^3) for 15 min, during which the mice were monitored for locomotion, exploration and anxiety parameters. On day three, for the sample trial, the mice returned to the open field in which two different objects had been set up beforehand. The animals were left free to explore them for 10 min, 5 h later, mice were again placed into the open field for the 10-min-duration test trial in which one of the objects previously explored had been replaced with a "new" one (the replaced objects across test trials were alternated to avoid a place preference bias). We chose a 5 h interval between sample and test trials because it represents a very challenging condition for the object memory of C57BL/6 mice (Sik et al., 2003). The exploratory activity toward each of the objects was videorecorded during both sample and test trials and later analyzed using the tracking software ANY-Maze (Stoelting Europe, Dublin, Ireland). The exploratory preference index was calculated for the test trial as (time spent exploring the novel object/total exploration time) x 100. The mice displaying a total exploratory time <10 s for both objects during the test trial were discarded from the analysis.

2.10. Spontaneous social interaction test

The spontaneous social interaction test investigated the behavior of two mice that were unfamiliar with each other and how they interacted in an open field. Briefly, a wild-type or a KI mouse was placed in an open-field (40 × 40 × 30 cm^3) and explored it for 20 min before an unknown control mouse of the same sex, age and genetic background was introduced into the chamber. Their interactions were then recorded for 5 min. Social behaviors such as approaching, contact (nose-to-nose, nose-to-anogenital), following, self-grooming and allogrooming were manually scored with the assistance of Ethovision video tracking system (Noldus, Wageningen, the Netherlands).

2.11. Electrophysiological recordings

Mice were anesthetized with 5% isoflurane and then decapitated. Brain was dissected out of the cranium and immediately immersed in ice-cold freshly prepared artificial cerebrospinal fluid (aCSF) containing, in mM: 119 NaCl, 11 D-glucose, 1.3 MgCl2.6H2O, 1.3 NaH2PO4, 2.5 KCl, 2.5 CaCl2, 26 NaHCO3, continuously oxygenated (95% O2, 5% CO2) (pH = 7.4) for a total duration of 3–4 min. Acute slices (350 μm thick) were prepared using a vibratome (VT 1000S; Leica Microsystems, Bannockburn, IL). Sections were incubated in standard aCSF supplemented with 100 μM Picrotoxin at room temperature for at least 1 h before recordings.

For recordings, a single slice was placed in the recording chamber (room temperature), submerged and continuously superfused with gassed aCSF (95% O2, 5% CO2; pH = 7.4) at a constant rate (2 ml min^{-1}) for the reminder of the experiment. Extracellular field excitatory postsynaptic potentials (fEPSPs) were recorded in the Dentate Gyrus (DG) using a glass micropipette filled with aCSF. fEPSPs were evoked by the electrical stimulation of the Perforant Pathway at 0.1 Hz (*i.e.*, a single pulse every 10 s) with a glass stimulating electrode (borosilicate capillary glass with filament, standard wall; OD:1.5 mm; ID:0.86 mm; Length: 75 mm; ref.: W3 30–0060 from Harvard Apparatus).

At the beginning of each experiment (when a stable fEPSP response is reached), Input/Output (I/O) curves were obtained by gradual increases in stimulus intensity (from 0 to 100 μA, 10 μA intervals) to assess changes in synaptic transmission. The same intensity of stimulation was kept for the reminder of the experiment.

Stable baseline fEPSPs was then recorded during 10 min by stimulating at 30% of maximal field amplitude (single pulse every 10 s, *i.e.*, 0,1 Hz). - Paired Pulse Ratios (PPR) were constructed to assess change in Short-Term plasticity. Two stimulations were applied with 50, 100, 150, 200, 300 and 400 ms interval.

LTP induction protocol by High-Frequency Stimulation (HFS): After a 10 min stable, a conditioning stimulus consisting in 3 train of 100-Hz stimulation was delivered to assess LTP. Following the conditioning stimulus, a 1 h test period was recorded where responses were again elicited by a single stimulation every 10 s (0,1 Hz) at the same stimulus intensity. Signals were amplified with an Axopatch 200B amplifier (Molecular Devices, Union City, CA) digitized by a Digidata 1322 A interface (Axon Instruments, Molecular Devices, US) and sampled at 10 kHz. Recordings were acquired using Clampex (Molecular Devices) and analyzed with Clampfit (Molecular Devices). Experimenters were blinded to treatment for all experiment.

2.12. Isolation of immune cells from adult mouse brains

Mice were deeply anesthetized with an intraperitoneal injection of ketamine (100 mg/kg)/xylazine (10 mg/kg)/ acepromazine (3 mg/kg). Immune brain cells were isolated from hippocampus and parahippocampus-enriched brain regions (perirhinal cortex, entorhinal cortex, presubiculum, parasubiculum, subiculum) as followed. Mice were transcardially perfused with ice-cold PBS (pH 7.4, 1 mg/ml EDTA). Brain tissue from adult mice was dissociated into single-cell suspensions using the Adult Brain Tissue Dissociation Kit in combination with the gentleMACS™ Dissociator with Heaters (Miltenyi Biotec, Paris, France). After dissociation, cell debris was removed using the Debris Removal Solution (Miltenyi Biotec, Paris, France). Brain immune cells were collected, washed and labeled for subsequent cell sorting and/or flow cytometry analysis.

2.13. Brain immune cell staining, flow cytometry and cell sorting

Staining of brain immune cell surface antigens was performed as previously described (Cazareth et al., 2014). Briefly, Fc receptors were blocked with 2.4G2 antibody. Cells were incubated with the appropriate combination of conjugated antibodies CD11b-PercP-Cy5.5, CD45-APC-Cy7, Ly6C-PE-Cy7, Ly6G-V450, CD3-FITC, MHC Class II-BV510 (BD Biosciences, Le Pont de Claix, France), ACSA-2-APC (Miltenyi Biotec, Paris, France) or isotype control antibodies for 30 min. Cells were washed and resuspended in PBS containing 0.5% BSA for analysis and cell sorting with FACS Aria III (BD Biosciences, Le Pont de Claix, France).

2.14. RNA isolation and quantitative PCR

Total RNA from hippocampus and parahippocampal brain regions were isolated using the Trizol® RNA extraction kit (ThermoFisher, Courtaboeuf, France) according to the manufacturer recommendations followed by a RQ1 DNAse (Promega, Charbonnières, France) treatment. First-strand cDNA were synthesized from 2 µg of total RNA with 200 U of SuperScript III reverse transcriptase (ThermoFisher, Courtaboeuf, France) in the appropriate buffer in the presence of 25 µg/ml random primers, 0.5 mM desoxyribonucleotide triphosphate mix, 5 mM dithiothreitol, 40 U RNAsin (Promega, Charbonnières, France). The reaction was incubated 5 min at 25 °C, then 50 min at 50 °C then inactivated 15 min at 70 °C. Quantitative PCR was performed using the SYBRgreen method (Roche Diagnostics, France) with the LightCycler 480 sequence detector system (Roche Diagnostics, France). Primers were purchased from QIAGEN (QuantiTect primer assay, QIAGEN, Courtaboeuf, France).

2.15. Cytokine measurement in CSF by CBA

Mice were anesthetized with an intraperitoneal injection of ketamine (100 mg/kg)/xylazine (10 mg/kg)/ acepromazine (3 mg/kg); then CSF (2–5 µl) was obtained by cisternal puncture. Cytokine and chemokine concentrations were measured using the V-PLEX Proinflammatory Panel 1 Mouse Kit according to the manufacturer's protocol (Meso Scale Discovery, Rockville, USA).

2.16. Immunohistofluorescence

Mice were treated with buprenorphine (0.1 mg/kg) and deeply anesthetized with xylazine/ketamine (15 mg/kg and 70 mg/kg respectively). Then, they were transcardially perfused with 50 ml of 0.9% NaCl, followed by 4% paraformaldehyde (PFA). Tissues were post-fixed in 4% PFA for 4 h and then cryoprotected in 30% sucrose for 48 h. Samples were snap-frozen in isopentane after cryoprotection with Cryomatrix (Thermo Scientific). For brain, 40-µm-thick free-floating serial coronal sections were sliced using cryostat.

For immunostaining, floating sections were incubated with antigen unmasking solution H3300 (Vector laboratories) for 10 min at 92 °C (Citrate buffer (pH 6)) and then sections were incubated in blocking buffer (0.5% Triton X-100, 5% normal goat serum, 4% bovine serum albumin (BSA)) for 1 h at RT. Staining was performed with primary antibodies diluted in blocking buffer overnight, at 4 °C. The following primary antibodies were used: Gfap, Iba1, PHB2, SLP2, eIF2α-P, TDP-43 and CHCHD10. The references of antibodies and the concentrations used are listed in Table 1. After several washings in PBS/Triton 0.1%, sections were incubated for 1 h, at RT, in a solution (PBS, 0.3% Triton X-100, 1% BSA) with the corresponding secondary antibodies conjugated to Alexa Fluor 488 or 594 (Thermo Fisher Scientific), listed in Table 1. Sections were rinsed in PBS/Triton 0.1% and PBS, and incubated with 4′,6-diamidino-2-phenylindole, dihydrochloride (DAPI) (2 µg/ml) (Life Technologies) for 5 min at RT. Finally, sections were mounted in Vectashield Hard Set medium (Vector Laboratories). All images were captured with a ZEISS LSM 880 or a ZEISS LSM 800 confocal laser-scanning microscope. The images were deconvolved with Huygens Essential Software™ (Scientific Volume Imaging) using a theoretically calculated point spread function (PSF) for each of the dyes. All selected images were iteratively deconvolved with maximum iterations scored 40 and a quality threshold at 0.05. The deconvolved images were used for

Table 1
Antibodies used in the study.

Antigen	Host	Source	Dilution
ACSA-2-APC	Human	Miltenyi Biotec # 130–116-245	FACS: 1/400
CD3e-FITC	Hamster	BD Biosciences # 553061	FACS: 1/400
CD11b-PercP-Cy5.5	Rat	BD Biosciences # 550993	FACS: 1/400
CD45-APC-Cy7	Rat	BD Biosciences # 561037	FACS: 1/400
CHCHD10	Rabbit	Sigma-Aldrich # HPA003440	IHF: 1/100
GFAP	Mouse	Proteintech # 60190–1-Ig	IHF: 1/200
Iba1	Rabbit	Wako # 019–19,741	IHF: 1/1000
IgG1-APC (REA control antibody)	Human	Miltenyi Biotec # 130–113-446	FACS: 1/400
IgG2a-BV510 (isotype control)	Rat	BD Biosciences # 562952	FACS: 1/400
IgG2a-V450 (isotype control)	Rat	BD Biosciences # 560377	FACS: 1/400
IgG2b-APC-Cy7 (isotype control)	Rat	BD Biosciences # 552773	FACS: 1/400
IgG2b-FITC (isotype control)	Hamster	BD Biosciences # 553062	FACS: 1/400
IgG2b-PercP-Cy5.5 (isotype control)	Rat	BD Biosciences # 550764	FACS: 1/400
IgM-PE-Cy7 (isotype control)	Rat	BD Biosciences # 560572	FACS: 1/100
Ly6C-PE-Cy7	Rat	BD Biosciences # 560593	FACS: 1/100
Ly6G-V450	Rat	BD Biosciences # 560603	FACS: 1/400
MHC Class II-BV510	Rat	BD Biosciences # 743871	FACS: 1/400
Fc Block 2.4G2	Rat	BD Biosciences # 553142	FACS: 1/200
Mouse IgG Alexa Fluor 488	Goat	Thermo Fischer # A11029	IHF: 1/500
PHB2	Mouse	Proteintech # 66424–1-Ig	IHF: 1/400
Phospho-eIF2α	Rabbit	Cell Signaling # 3398	IHF: 1/200
Rabbit IgG Alexa Fluor 594	Donkey	Thermo Fischer # A21207	IHF: 1/500
SLP2	Rabbit	Proteintech # 10348–1-AP	IHF: 1/100
TDP-43	Mouse	Proteintech # 67345–1-Ig	IHF: 1/400

IHF: ImmunoHistoFluorescence, FACS: Flow Cytometry.

quantitative cytoplasmic TDP-43 inclusion analysis with Huygens Essentiel Software™ with the following standardized set of parameters: threshold = 10%, seed = 10%, garbage = 20 and remove round objects with axial sphericity threshold = 0.4 or 0.5 for the hippocampus or the entorhinal cortex respectively.

2.17. TUNEL assay

Brain tissues from animals perfused with 4% PFA were cut into 40 µm sections and stained with the *In Situ* Cell Death Detection Kit, Fluorescein (Roche). Briefly, sections were treated with antigen unmasking solution H3300 (Vector laboratories) for 20 min at 92 °C, washed in PBS and blocked for 60 min in Tris-HCL 0.1 M pH 7.5, 3% BSA, 20% normal goat serum, 0.1% Triton. Sections were mounted onto glass slides and reaction mix containing fluorescein-dUTP and terminal deoxynucleotidyl transferase (TdT) was applied for 60 min at 37° C. A set of sections was incubated in the absence of TdT as a negative control. After PBS washes and counterstain with DAPI 2 µg/ml for 5 min, sections were washed again in PBS. Images were captured with a ZEISS LSM 800 confocal laser-scanning microscope.

2.18. Statistical analysis

Wherever possible, we grouped males and females of the same genotype. To ensure that this grouping was legal, we observed the graphical dispersion of individuals (Supplementary Figs. 1, 2 and 3) and subjected our data to two-way ANOVAs (genotype x sex). In the event of a significant genotype x sex interaction, we performed separate analyses for males and females (grip strength and open-field tests) (Supplementary Fig. 4).

For behavioral studies, the statistical analyses were conducted using the InVivoStat software (Clark et al., 2012) or GraphPadPrism (Graphpad Software). We applied factorial ANOVA followed by Holm's test for post-hoc comparisons to most of the data. For the other ones, either *t*-test or Mann-Whitney test was used, depending if the parametric conditions were met or not. The normality of residuals was assessed with normal probability plots and homoscedasticity with standardized residuals *vs* fitted values plot.

For immunofluorescence, statistical analyses were performed with Mann-Whitney's test. The quantitative data were analyzed in Microsoft Excel and GraphPad Prism (GraphPad Software). Data are means ± SEM. "n" represents number of mice per experiment. The data from *Chchd10*$^{S59L/+}$ mice were compared to the control littermates. *P*-value = * < 0.05, ** < 0.01, *** < 0.001 and **** < 0.0001. ns = not significant.

3. Results

3.1. Evaluation of *Chchd10*$^{S59L/+}$ mice reveals no major motor disability at 5 and 10 months of age

Few cognitive tests are suitable for motor impaired animals. *Chchd10*$^{S59L/+}$ (KI) mice started developing motor dysfunction after 8 months of age (Anderson et al., 2019; Genin et al., 2019). To ensure that cognitive phenotypes could not be obscured by neuromuscular defects in *Chchd10*$^{S59L/+}$ mice, we analyzed several aspects of motor functions of the animals at 5 and 10 months of age. *Chchd10*$^{S59L/+}$ mice showed no motor deficits during rotarod, pole and parallel rod floor tests (Fig. 1a-g). Only the grip strength and actimetry tests revealed slight deficits in KI mice at 10 months. The grip strength results showed a decrease in the forelimb strength of 10-month-old KI female mice only (Fig. 1e). The actimetry test, which measures spontaneous locomotor activity, showed a slight rearing deficiency in KI 10-month-old mice compared to WT animals (Fig. 1h-o). These results are compatible with the onset of a motor deficit from 8 to 10 months, which will worsen until the animals are killed at around 12–14 months (end stage), due to their cardiac decompensation. They validate the choice of behavioral tests used in the rest of this study.

3.2. *Chchd10*$^{S59L/+}$ mice show normal spatial memory but impaired recognition memory capacities and altered anxiety-related behaviors

To determine whether expression of the heterozygous S59L variant in mouse leads to the defects found in FTD patients, we analyzed performances of the animals, at 5 and 10 months of age, in behavioral tests designed to assess various aspects of their cognitive abilities. The Barnes maze is designed for testing spatial memory. No behavioral differences were observed between *Chchd10*$^{S59L/+}$ mice and control littermates (Fig. 2a-h). Indeed, KI mice learn and remember the target location in the same way as WT animals. We then used the novel object recognition test (NORT), which is based on measuring the spontaneous preference for novelty in rodents, to assess recognition memory. As shown in Fig. 2k-l, the 5- and 10-month-old WT animals spent significantly more time in front of the novel object during the test phase. Conversely, the 5-month-old KI mice did not spend any more time in front of the new object (Fig. 2k). At 10 months, they spent even less time in front of the novel object (Fig. 2l), thus suggesting abnormalities in object recognition memory of KI animals. Open-field and elevated plus maze (EPM) tests, used to assess anxiety-related behavior, also revealed differences between *Chchd10*$^{S59L/+}$ mice and control littermates (Fig. 3a-d). Open-field is one of the only tests we've carried out that revealed an age-dependent interaction between mouse sex and genotype. In this test, 5-month-old KI female mice spent a higher percentage of time in the center of the arena as compared to their WT female littermates, suggesting less anxiety. 10-month-old KI male mice make more entries into the open-field center than WT male controls in relation to the distance they travel, suggesting less anxiety. In the EPM test, 5-month-old KI mice made fewer entries in the open arm than WT animals, indicating more anxious traits. These observations suggest anxiety-linked behavioral changes in KI mice which, depending on sex, manifest themselves at different ages. No difference was observed in spontaneous social interaction tests between KI and WT animals (Fig. 3e-j).

3.3. Long Term Potentiation induced by high frequency stimulation is impaired in *Chchd10*$^{S59L/+}$ mice

NORT results indicate a defect in non-spatial learning of object identity in *Chchd10*$^{S59L/+}$ mice. The perirhinal cortex belongs to the parahippocampal regions that provide sensory inputs to the dentate gyrus of the hippocampus through lateral entorhinal cortex. Therefore, we performed electrophysiological analysis of long-term potentiation (LTP) at the Perforant Pathway-Dentate Gyrus (PP-DG) synapses in brain slices from *Chchd10*$^{S59L/+}$ mice and control littermates, aged 5 or 10 months (Fig. 4a). High frequency stimulation (HFS) of the PP resulted in robust LTP in slices from WT mice but clearly revealed impaired LTP in those from *Chchd10*$^{S59L/+}$ mice at 10 months of age (Fig. 4b-e). At 10 months, KI mice also showed a lower amplitude of post-tetanic potentiation (PTP) at PP-DG synapses, suggesting altered short-term plasticity. One explanation could be that the S59L mutation in *CHCHD10*, which leads to disorganization of mitochondrial cristae and disassembly of the MICOS complex, could result in defects in the storage and/or release of intramitochondrial Ca^{2+}, potentially impacting presynaptic plasticity.

Electrophysiological analysis also showed normal basal synaptic transmission (Fig. 4f, g) and paired-pulse ratios (Fig. 4h, i) at PP-DG synapses of *Chchd10*$^{S59L/+}$ mice.

3.4. Integrated stress response (ISR) activation is associated with SLP2/PHB2 aggregates in the hippocampus but not in the entorhinal cortex of *Chchd10*$^{S59L/+}$ mice

At the end-stage of the disease, *Chchd10*$^{S59L/+}$ mice display typical ALS features in spinal cord MNs. However, in ALS, the presence of

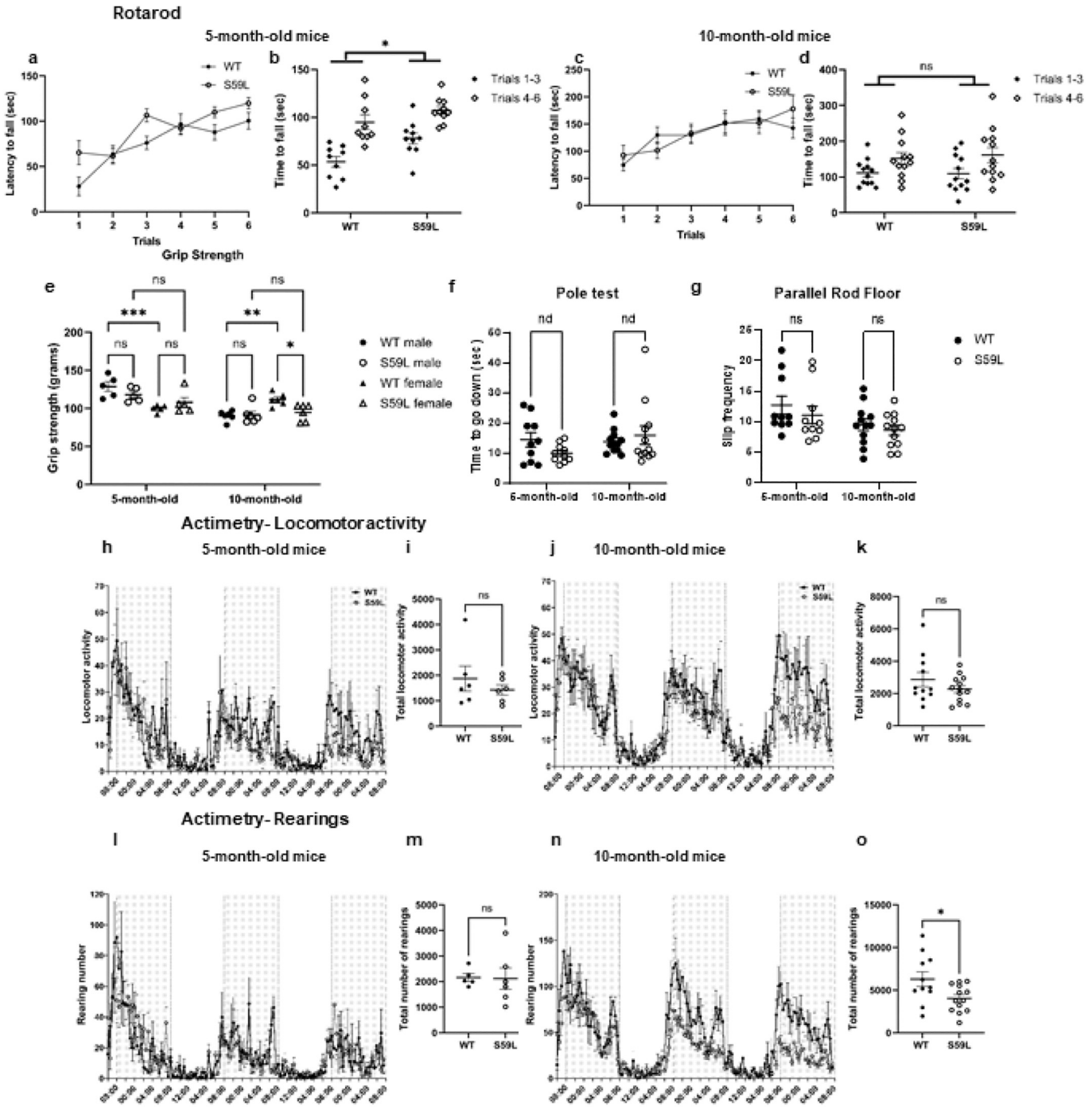

Fig. 1. Motor function assessment of *Chchd10*$^{S59L/+}$mice reveals mild late-onset deficits.

a-d, Rotarod performance was evaluated on 5- (**a, b**) and 10-month-old (**c, d**) wild-type (WT) and *Chchd10*$^{S59L/+}$ (S59L) mice. **a, c,** Latency to fall was measured across 6 consecutive trials. **b, d,** Mean latency to fall in seconds was calculated for the first 3 and the last 3 trials. Data were analyzed by 3-way ANOVA (genotype x sex x trial) and show that 5-month-old KI mice, overall, perform better than WT mice, but that their learning capacity in the rotarod task is identical. No further difference in 10-month old mice was observed. **e-g**, Grip strength (**e**), pole test (**f**) and parallel rod floor (**g**) were performed on 5- and 10-month-old WT (black) and S59L (white) male and female mice. **e,** Forelimb grip strength was performed to measure to neuromuscular function of 5- and 10-month-old WT male (black dots), WT female (black triangles) and *Chchd10*$^{S59L/+}$ male (white dots) and female (white triangles) mice. Results are expressed in grams and are the average of 3 trials per mouse. They reveal differences between 5-month and 10-month-old WT male and female mice as well as a slight decrease in grip strength of 10-month-old KI female mice. **f,** Basal ganglia related movement deficits were evaluated through the pole test. Results show the latency to go down recorded in seconds and are the average of 3 trials per mouse. **g,** The parallel rod floor test was used to estimate the motor coordination of *Chchd10*$^{S59L/+}$ mice. Results show the number of foot slip errors recorded over a period of 5 min (slip frequency). Results are presented as mean ± standard error of the mean (SEM) and show no significant differences between WT and S59L mice. ns, non significant. $N = 5–6$. **h-o,** Actimetry was recorded over a 3-day period. **h, j,** The curves at the top represent the back-and-forth activity of the mice (WT, black curve and S59L, gray curve). **i, k**, Total locomotor activity represents the number of back-and-forth recorded over the 3-day period. **l, n,** The curves represent rearing activity (WT, black curve and S59L, gray curve). **m, o**, The total number of rearings was counted over the recording period and shows a deficit in 10-month-old S59L mice. Results reveal a slight deficit in the righting ability of 10-month-old S59L mice. Results are presented as mean ± SEM. * Significance to control. *$p < 0.05$; ns, non significant. $N = 5–6$. Detailed statistical test results are available in Sup. Fig. 4.

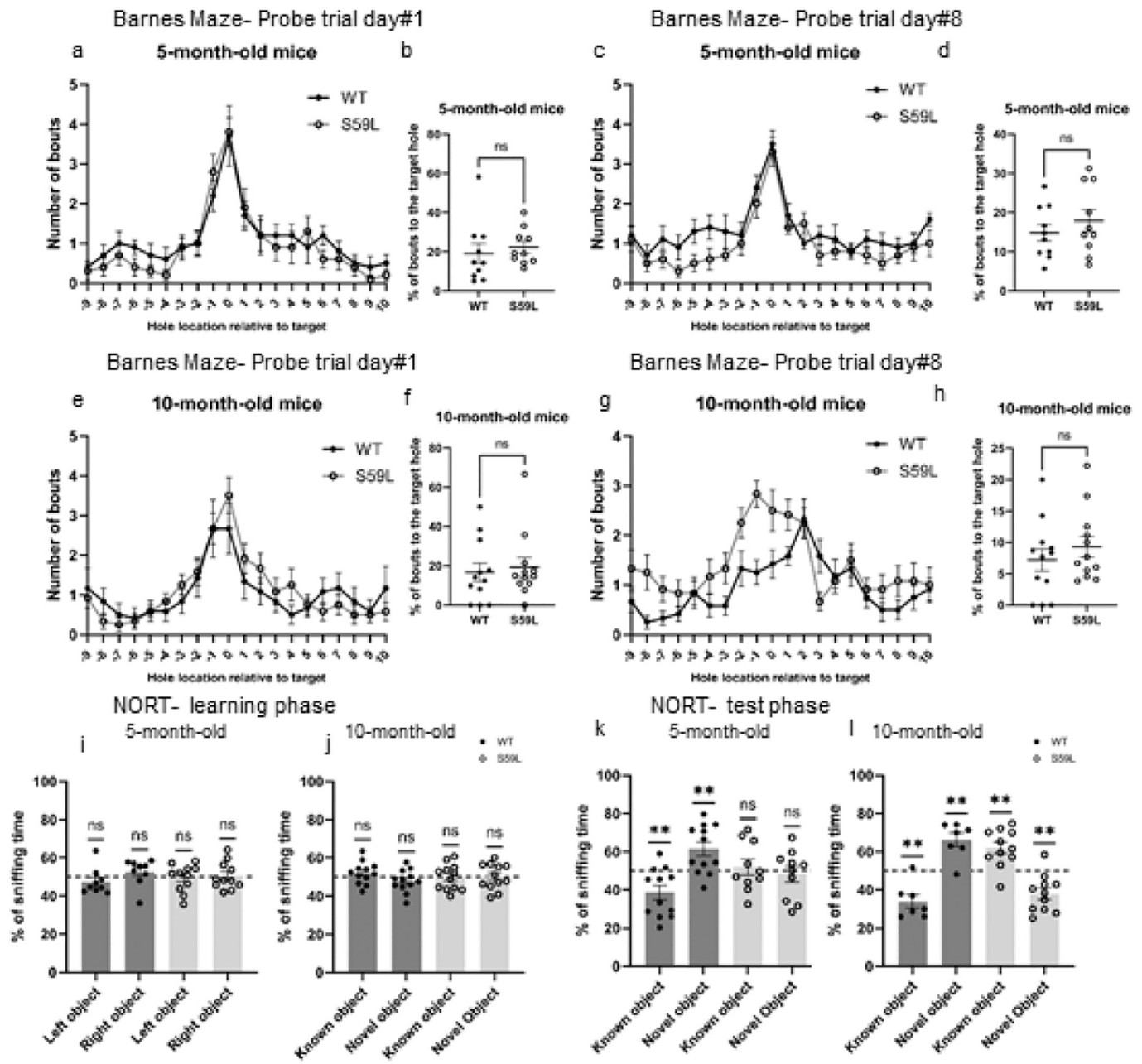

Fig. 2. *Chchd10*$^{S59L/+}$mice have normal spatial memory but show deficits in the novel object recognition test.
a-h, Barnes Maze test: Spatial memory acquisition and retention were evaluated on 5- (**a-d**) and 10-month-old (**e-h**) WT (black dots) and S59L (white dots) male and female mice. Probe trials at day 1 (**a, b, e, f**) and day 8 (**c, d, g, h**) after the learning sessions. **a, c, e, g,** show the number of exploration bouts that were recorded at the location of the target hole (defined as position 0) as well as each individual non-target hole. The absolute value of the "hole number relative to target" reflects the distance from the target hole (WT, black curve and S59L, gray curve). **b, d, f, h,** Percentage of bouts to the target hole was calculated as (the number of bouts to the target hole to the total number of bouts to all holes) x 100. Results show no significant difference between WT and S59L mice performances in spatial memory acquisition and retrieval. **i-l, NORT:** NORT protocol consisted of two 15 min habituation sessions to the open-field on days 1 and 2. **i-j,** On day 3, two identical objects were placed in the arena and 5- (**i**) and 10-month-old (**j**) WT (black dots) and S59L (white dots) mice were allowed to explore for 10 min (learning phase). **k-l,** After 5 h, one object was replaced by a new one for the test phase and 5- (**k**) and 10-month-old (**l**) WT (black dots) and S59L (white dots) mice were allowed to explore for 10 min. The dotted line represents the theoretical expected 50% of time that mice should spend exploring each object. Histograms represent the percentage of time sniffing each object for each experimental group during the learning and test phases. Results reveal deficits in object recognition for both 5- and 10-month-old S59L mice. Values are shown as mean ± SEM; $^{**}p < 0.01$; ns, non significant. $N = 7$–11. Detailed statistical test results are available in Sup. Fig. 4.

protein aggregates is not restricted to the spinal cord and different brain region as the hippocampus can be affected. We carried out a neuropathological analysis of the hippocampus in these animals. We previously described a novel type of aggregates in *Chchd10*$^{S59L/+}$ mice, composed of Stomatin-Like Protein 2 (SLP2) and prohibitins (PHB1 and PHB2), key proteins in the inner mitochondrial membrane (IMM) organization (Mitsopoulos et al., 2015; Signorile et al., 2019). We found a significant accumulation of SLP2/PHB2 aggregates in DG, as shown on the lower panel of Fig. 5a, and *cornus ammonis* (CA) from *Chchd10*$^{S59L/+}$ mice at the end-stage compared with WT littermates (Genin et al., 2022). As axons from the PP convey sensory information from neurons of the entorhinal cortex to the DG (Fig. 4a), we also performed immunostaining with antibodies against SLP2 and PHB2 on entorhinal cortex regions from *Chchd10*$^{S59L/+}$ and WT mice at 10 months of age without

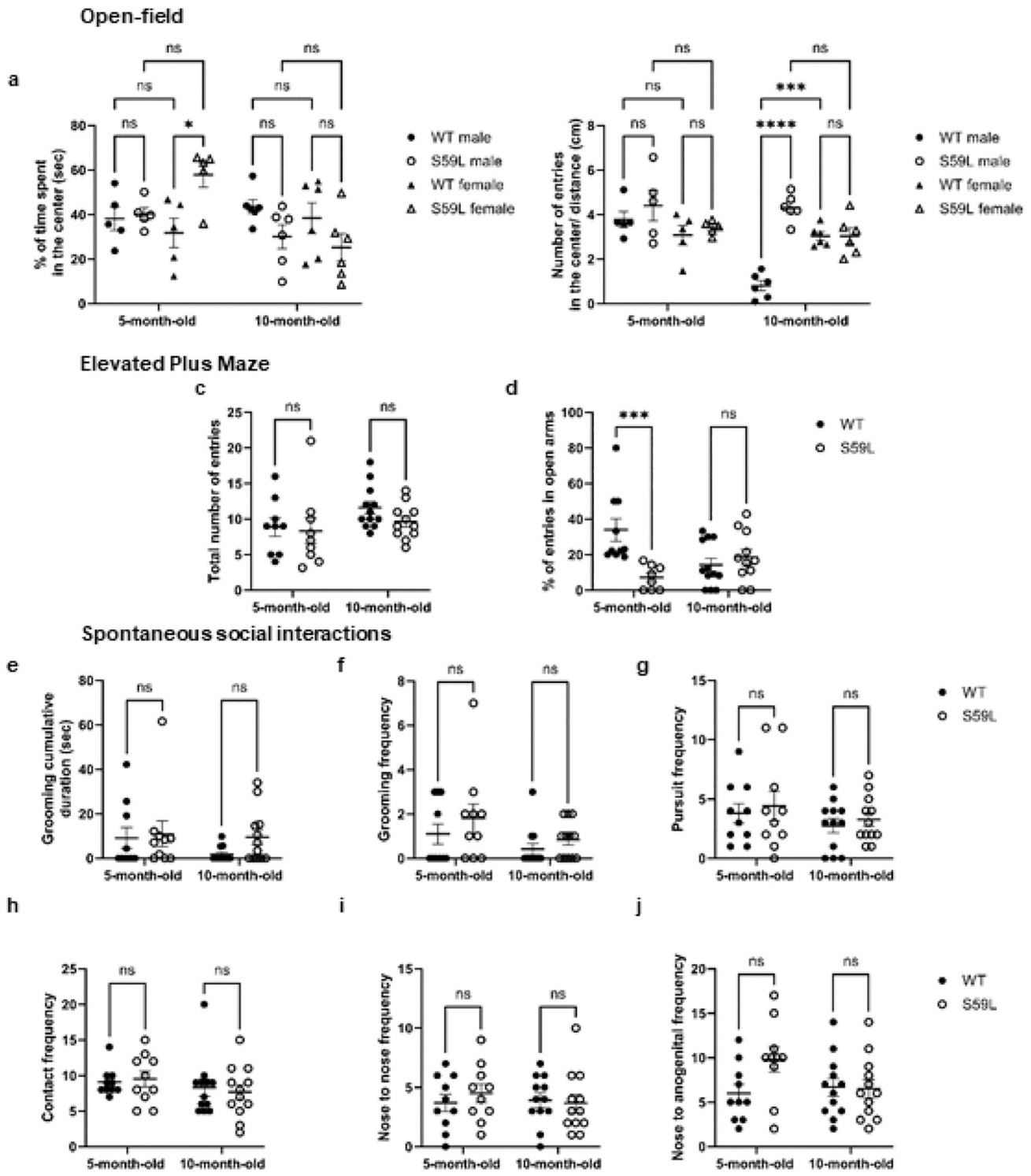

Fig. 3. Anxiety-related behavior tests reveal alterations in *Chchd10*$^{S59L/+}$ mice.
Anxiety-related behaviors were estimated by the open-field (**a-b**) and the elevated plus maze (**c-d**) tests. **a-b,** Behaviors in the open-field test were recorded for 10 min. **a,** Results show the percentage of time spent in the aversive center of the arena by WT (black dots), S59L (white dots) male mice and by WT (black triangles), S59L (white triangles) female mice at 5 and 10 months of age. **a**, Results show the % of time spent in the center of the arena and suggest that 5-month-old S59L female mice spend more time in the aversive zone of the open-field than the WT female control mice. **b,** Results show the total number of entries in the center related to the total distance covered and indicate that 10-month-old S59L male mice make more entries in the center of the open-field that the WT male control mice. **c-d,** Behaviors in the elevated plus maze test were recorded for 5 min. **c**, Results show the total number of entries in the open arms performed by WT (black dots) and S59L (white dots) mice at 5 and 10 months of age. **d**, Results show the percentage of entries in the open arms performed by mice and indicate that 5-month-old S59L mice make less entries in the open arms than the WT mice. **e-j,** Social interaction test: 5- and 10-month-old WT (black dots) and S59L (white dots) mice were subjected to a 20 min exploratory session before the social interaction session of 5 min with an unknown mouse of the same sex, age and genetic background. Grooming cumulative duration (**e**), grooming (**f**), pursuit (**g**), contact (**h**), nose-to-nose (**i**) and nose-to-anogenital (**j**) frequencies were scored. Results indicate that S59L mice have unaltered spontaneous social interactions as compared to WT mice. *** $p < 0.005$; ns, non significant. $N = 5–6$. Detailed statistical test results are available in Sup. Fig. 4.

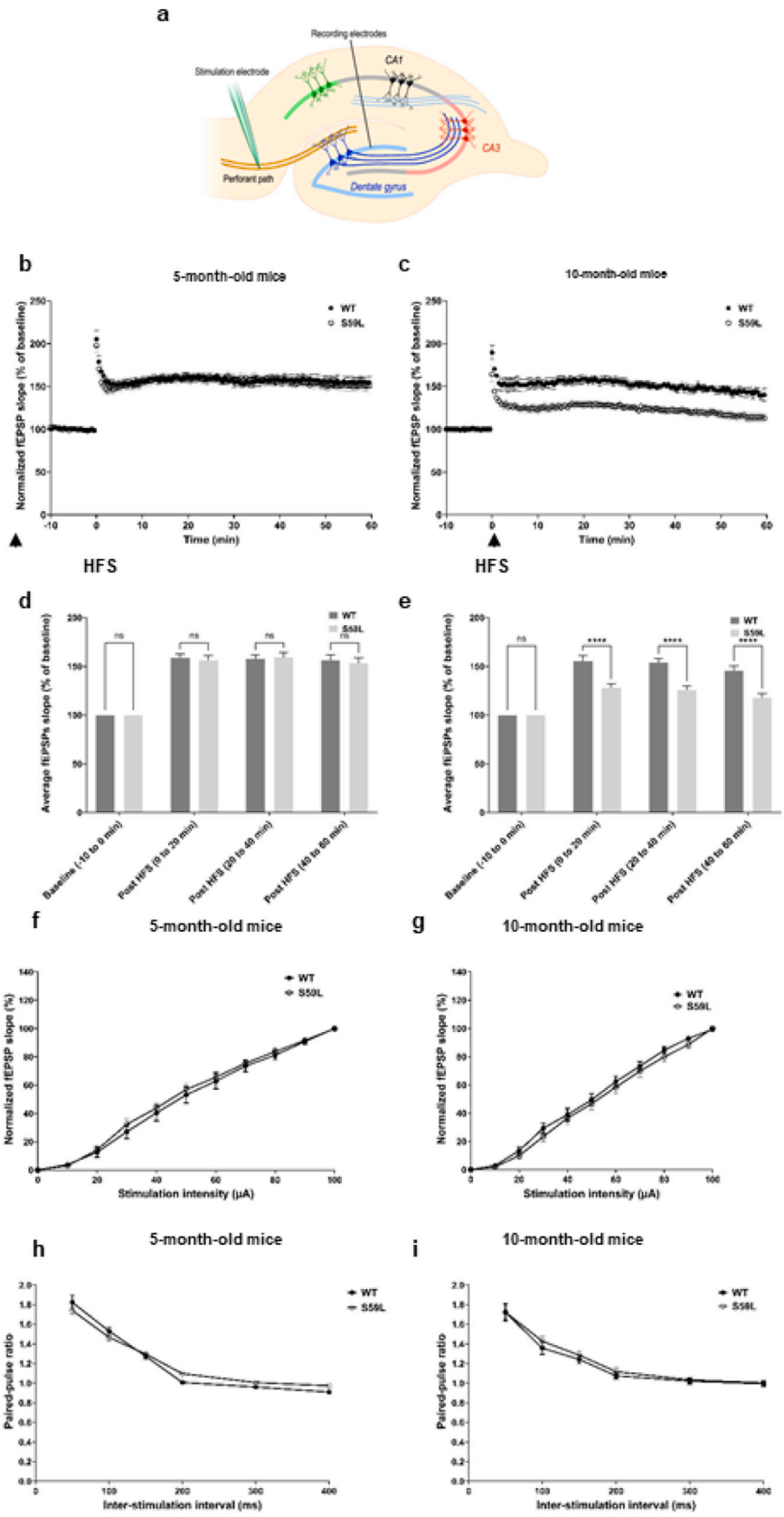

(caption on next page)

Fig. 4. Assessment of the hippocampal long-term potentiation (LTP) at performant pathway-dentate gyrus synapses (PP-DG) reveals late-onset deficits in *Chchd10*$^{S59L/+}$mice.

a, Schematic representation of the protocol. The stimulating electrode was located in the perforant pathway from the entorhinal cortex and the recording electrode was implanted in the dentate gyrus of the hippocampus. **b, c,** Results show the time course of the average slope of elicited field responses following LTP induction by a high frequency stimulation (HFS) induction protocol (3*100 Hz) at the PP-DG synapses from 5- (**b**) and 10- (**c**) month-old male and female S59L (white dots) mice and their wild-type littermates (WT, black dots). Time-point 0 represents delivery of HFS, as indicated by an arrow. Slopes of fEPSP are normalized to the baseline and plotted against time. The data are represented as means ± SEM. **e,** Columns represent the average slope response during baseline (−10 to 0 min), 0–20 min post-LTP induction, 20–40 min post-LTP induction and 40–60 min post-LTP induction for 5- (**d**) and 10- (**e**) month-old WT and S59L mice. LTP was measured as percent of baseline fEPSP slope recorded over a 10-min period before LTP induction. This value was taken as 100% of the excitatory post-synaptic potential slope and all recorded values were normalized to this baseline. Results show that LTP is impaired in 10-month old S59L mice, when compared to littermates. **f, g,** Evoked response amplitudes were recorded from the DG in response to increasing stimulating currents (50 to 100 μA) to the PP. Normalized average slope of fEPSP evoked during input-output responses were recorded at the perforant pathway-dentate gyrus (PP-DG) synapses from 5- (**f**) and 10-month-old (**g**) WT (black dots) and S59L (white dots). **h, i,** Paired-pulse facilitation of fEPSPs were recorded at the PP-DG synapses from 5- (**h**) and 10-month-old (**i**) WT (black dots) and S59L (white dots). The paired-pulse ratio was measured at stimulus intervals of 50, 100, 150, 200, 300 and 400 ms. Results show that S59L mice have unaltered basal synaptic transmission and short-term plasticity at the PP-DG synapses. The data are represented as means ± SEM. * $p < 0.05$; ** $p < 0.01$; ns, non significant. $N = 5$–6.

finding SLP2/PHB2 aggregates (Fig. 5a). We also observed that SLP2/PHB2 aggregates were associated with increased cell death in DG, as shown on the lower panel of Fig. 5b, and CA areas of *Chchd10*$^{S59L/+}$ animals (Genin et al., 2022). However, TUNEL analysis did not reveal an increase of apoptosis in the entorhinal region of these mice (Fig. 5b-c). It has been proposed that protein aggregation triggers the mitochondrial integrated stress response (mtISR) found in *CHCHD10*-related disease (Anderson et al., 2019). Since ISR activation is based on phosphorylation of the eukaryotic translation initiation factor eIF2, we analyzed the expression of phosphorylated eiF2 (eiF2α-P) in the hippocampus and in the entorhinal cortex of *Chchd10*$^{S59L/+}$ and WT mice. Quantitative analysis revealed a significant increase of eiF2α-P expression in these brain areas from *Chchd10*$^{S59L/+}$ mice compared to control littermates (Fig. 5d-e). It has been shown that TDP-43 and CHCHD10 aggregates co-localize in mouse and patient brains (Liu et al., 2022). We found TDP-43 and CHCHD10 in the same cytoplasmic inclusions in the hippocampus (CA) of *Chchd10*$^{S59L/+}$ mice at 10 months (Fig. 6).

3.5. Neuroinflammation in the hippocampus and entorhinal cortex of *Chchd10*$^{S59L/+}$ mice

Neuroinflammation is a common feature in ALS/FTD, primarily characterized by activation of innate immune sensing pathways in microglia and astrocytes resident to the central nervous system (CNS). The first cells to respond are likely microglia, as they are exquisitely sensitive to any perturbation in their environment. We analyzed the expression of the actin-binding protein (Iba1) on hippocampus and entorhinal cortex sections from *Chchd10*$^{S59L/+}$ mice and WT animals at 10 months of age. Immunostaining with antibodies against Iba1 revealed microglial activation in *Chchd10*$^{S59L/+}$ brains compared with WT (Fig. 7a). We analyzed the expression of the astrocytic marker GFAP in the same brain regions. Quantitative analysis revealed a significant increase of anti-GFAP immunostaining signals in the DG but not in the entorhinal cortex of *Chchd10*$^{S59L/+}$ animals compared with control littermates (Fig. 7b).

According to these results, we found an upregulation of surface marker RNA expression (astrocytic GFAP, microglial CD11b and CX3CR1) in the hippocampus of *Chchd10*$^{S59L/+}$ mice (Fig. 8a), and of pro-inflammatory cytokine (IL-1β, IL-6, TNF-α) gene expression in microglia of the animals (Fig. 8b). In ALS and FTD patients, analysis of CSF revealed altered secretions of inflammatory cytokines and chemokines such as SDF-1α (also known as CXCL12) (Andrés-Benito et al., 2020), as observed in our mouse model at 10 months of age (Fig. 8e). Interestingly, this chemokine also appeared to be significantly elevated in the plasma of KI mice at the same age (Fig. 8d). CNS-border-associated macrophages (BAMs) are found at brain border structures and are important in regulating the exchange of molecules between the brain and peripheral tissues. They include several types of macrophages, such as meningeal macrophages, perivascular macrophages (PVMs), and choroid plexus macrophages. Although single-cell profiling studies revealed the heterogeneity of BAMS, they are often identified by their higher expression of CD45 surface marker (CD11b + CD45high), as compared to microglia (CD11b + CD45low) (Fig. 8f). While the role of BAMs in neurodegenerative disease remains unknown, they have been shown to support blood vessel repair, mediate blood–brain barrier permeability, produce reactive oxygen species, secrete chemokines to orchestrate monocyte and granulocyte recruitment, and are highly phagocytic, indicating they may play a role in disease pathogenesis as effectors or regulators of immune responses. Here we show that BAMS from *Chchd10*$^{S59L/+}$ animals express higher levels of IL-6 and TNF-α mRNAs as compared to their WT littermates (Fig. 8c), that could be involved in the recruitment of circulating immune cells, such as lymphocytes, neutrophils and inflammatory monocytes by altering the integrity of blood-brain barrier (BBB) (Fig. 8 g).

4. Discussion

The identification of the *CHCHD10* gene in ALS patients was the first genetic evidence that a mitochondrial defect may be the cause of MND (Bannwarth et al., 2014). To understand how mitochondrial dysfunction can lead to neuronal death, we generated a mouse model expressing the deleterious variant (S59L) identified in our original family. *Chchd10*$^{S59L/+}$ mice die prematurely (before 14 months of age) from mitochondrial cardiomyopathy. Nevertheless, at the end stage of the disease, they show typical MND features: fragmentation of neuromuscular junctions, TDP-43 proteinopathy and a 16% reduction in spinal motor neurons; this decrease being clearly insufficient to cause major motor disability (Genin et al., 2019). The aim of this study was to determine whether *Chchd10*$^{S59L/+}$ mice also reproduce the signs of FTD, found in patients expressing the same *CHCHD10* variant. By using NORT, we show that both male and female KI animals present impaired episodic-like memory as early as 5 months of age. Memory impairment was demonstrated by NORT in several FTD mouse models, such as transgenic mice over-expressing TDP-43 in the forebrain (CaMKII-TDP-43 Tg mice) (Tsai et al., 2010) or K3 animals that express the K369I human tau variant in neurons (Ittner et al., 2008); for review see (Ahmed et al., 2017). The learning and memory deficiency in FTD patients is a key factor leading to social behavior and language disorders. In *Chchd10*$^{S59L/+}$ mice, NORT is impaired in young animals, while protein aggregates are not yet found in the hippocampus (Genin et al., 2022). These results show that some memory defects are early events in the pathological cascade leading to FTD in *Chchd10*$^{S59L/+}$ mice also. The entorhinal cortex is located in the medial temporal lobe and serves as a crucial interface between the neocortex and the hippocampus, through the PP. In various types of dementia, including Alzheimer's disease (AD), there is evidence of early and significant damage to the entorhinal cortex and PP. Here, both electrophysiological measurements at synapses between the PP and DG and neuropathological analyses validate the impairment of this crucial brain region in *Chchd10*$^{S59L/+}$ mice.

Anxiety-related behavior tests also revealed alterations in

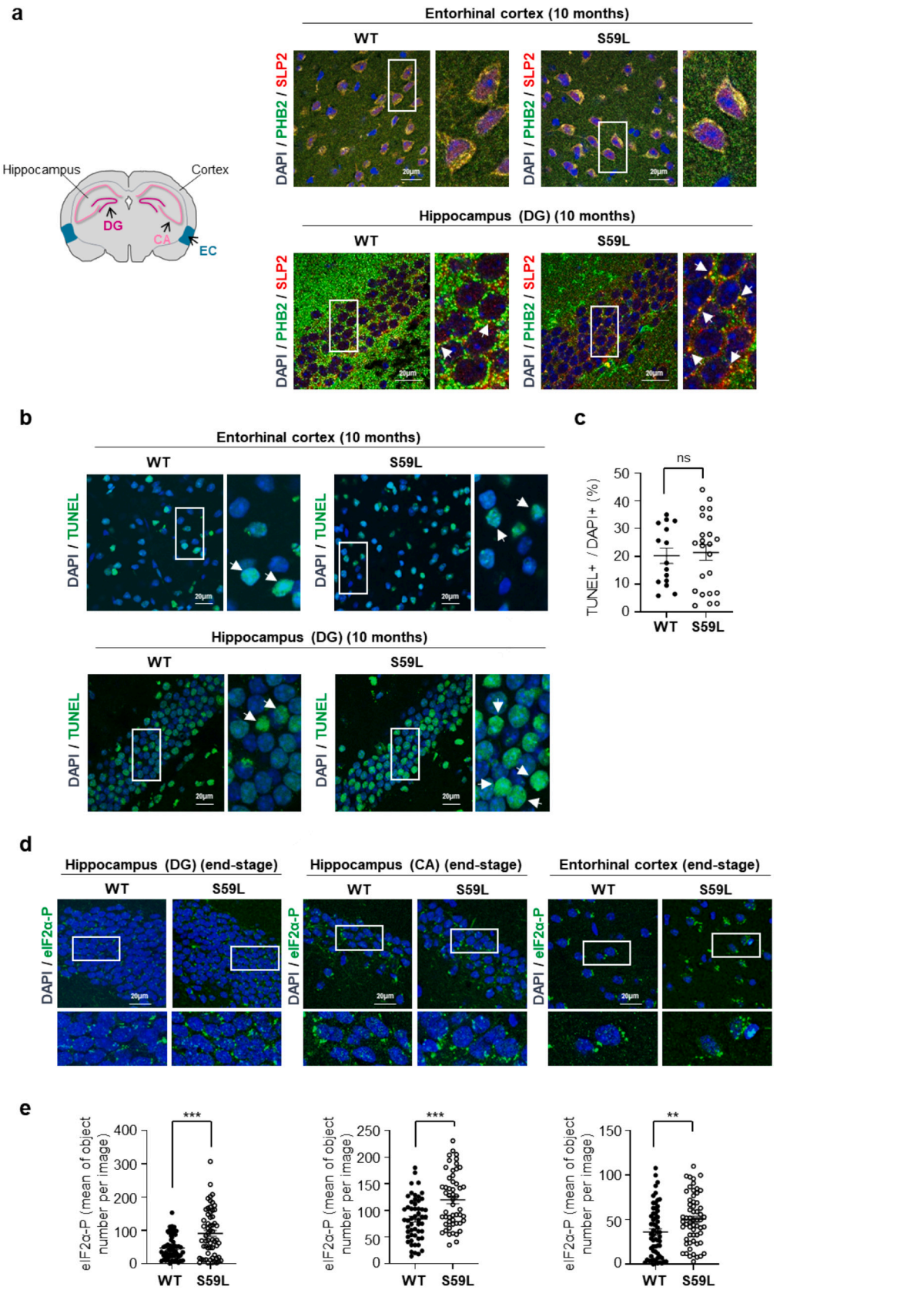

(caption on next page)

Fig. 5. SLP2/PHB2 aggregates and activation of mtISR in *Chchd10*$^{S59L/+}$ mice. a, Absence of SLP2/PHB2 aggregates in the entorhinal cortex (EC) of *Chchd10*$^{S59L/+}$ mice. Brain sections visualizing the entorhinal cortex from *Chchd10*$^{S59L/+}$ mice (S59L/+) and control littermates (WT) at 10-month-old. Immunolabeling was performed with antibodies against SLP2 (red) and PHB2 (green). Scale bar = 20 μm. The lower panel shows the presence of these aggregates (arrows) in the DG of *Chchd10*$^{S59L/+}$ mice at 10 months (Genin et al., 2022). **b-c,** No increase of apoptosis in the entorhinal cortex of *Chchd10*$^{S59L/+}$ mice. **b,** TUNEL staining of brain sections visualizing the entorhinal cortex from *Chchd10*$^{S59L/+}$ mice (S59L/+) and control littermates (WT) at 10-month-old. Arrows indicate apoptotic (TUNEL+/DAPI+) cells. Scale bar = 20 μm. **c,** Quantification of TUNEL positive cells observed in **b**. $n = 3$ independent experiments with 3 *Chchd10*$^{S59L/+}$ mice and 3 control littermates. For each animal, 2 to 4 fields (at least 4 images per field) were randomly selected and analyzed for scoring TUNEL-positive cells *versus* total number of nuclei. Values are mean ± SEM. The lower panel shows the increase of apoptotic cells (arrows) in the DG of *Chchd10*$^{S59L/+}$ mice at 10 months (Genin et al., 2022). **d-e,** Increase of phosphorylated eiF2 (eiF2α-P) expression in the hippocampus and the entorhinal cortex of *Chchd10*$^{S59L/+}$ mice at end-stage. Brain sections visualizing hippocampal areas: DG (left panel) and CA (middle panel) and the entorhinal cortex (right panel) were labeled with antibodies against eiF2α-P (green). Scale bar = 20 μm. Quantification of eiF2α-P staining observed in **d**. $n = 3$ independent experiments with 3 *Chchd10*$^{S59L/+}$ mice and 3 control littermates. The data are represented as means ± SEM. *P*-value = ** < 0.01, *** < 0.001, ns = not significant. (For interpretation of the references to colour in this figure legend, the reader is referred to the web version of this article.)

Chchd10$^{S59L/+}$ animals. It cannot be ruled out that memory dysfunction may contribute to this behavior disturbance. Nevertheless, these behavioral abnormalities are frequently found in mouse models of FTD and anxiety symptoms are highly prevalent among people with dementia (Ahmed et al., 2017) (Benussi et al., 2021).

Protein aggregation in degenerating neurons is a hallmark of FTD, ALS and other neurodegenerative diseases. The aggregates observed in *Chchd10*$^{S59L/+}$ mice include proteins such as TDP-43, CHCHD10 and its paralog CHCHD2 (Anderson et al., 2019) (Genin et al., 2019) (Shammas et al., 2022). We also found a new type of aggregates including SLP2 and PHB proteins, which do not co-localize with CHCHD10 inclusions. SLP2/PHB small aggregates are associated with an increase of apoptosis in the hippocampus of *Chchd10*$^{S59L/+}$ mice at end-stage compared with WT littermates (Genin et al., 2022). Protein aggregation is at least in part responsible for mtISR activation reported in the heart tissue from KI mice carrying *CHCHD10* variants (Anderson et al., 2019) (Shammas et al., 2022). The phosphorylation of eIF2 results in a general reduction in protein synthesis and reprogramming specific gene expression in response to internal or environmental stresses. SLP2 and prohibitins control the activity of proteases such as OMA1 (Wai et al., 2016) (Steglich et al., 1999). In *Chchd10*$^{S59L/+}$ mouse heart tissue, we have shown that SLP2/PHB aggregates are associated with an instability of the PHB complex in the inner mitochondrial membrane at least in part responsible for the activation of the OMA1 cascade. OMA1 cleaves DELE1, the short form of which is released into the cytoplasm and activates HRI, one of four eIF2α kinases (Fessler et al., 2022). Several studies demonstrated that *CHCHD10* mutations induce mtISR activation *in vivo*, likely by different mechanisms including protein aggregation and OMA1 activation (Anderson et al., 2019) (Shammas et al., 2022). Activation of the mtISR in the entorhinal cortex of 10-month-old KI mice in the absence of protein aggregates could suggest that these aggregates play a greater role in perpetuating stress than in triggering it.

The brain is one of the most sensitive organs to alterations in the ISR, which are involved in cognitive deficits and neurodegenerative pathologies (for review see (Costa-Mattioli and Walter, 2020)). Numerous reports have demonstrated that ISR is a molecular control center regulating the switch from short to long term memory (Costa-Mattioli et al., 2007) (Trinh and Klann, 2013) (Chesnokova et al., 2017). Long-term potentiation (LTP) is a persistent increase in synaptic strength following high frequency stimulation. The late phase of LTP (L-LTP) is involved in the formation of long-term memory that requires *de novo* protein synthesis to establish stronger synaptic connections. ISR activation impairs long-term memory formation by preventing the synthesis of proteins required for synaptic modification (Costa-Mattioli et al., 2007). The increase of eiF2α-P expression that we found in the hippocampus of *Chchd10*$^{S59L/+}$ mice confirms that mtISR activation is likely in part responsible for the impairment of memory and learning found in these animals. The presence of phosphorylated eIF2 has also been reported in post-mortem brains of patients affected by neurodegenerative disorders, including ALS or AD (Moon et al., 2018). ISR activation is thought to be beneficial in stress situations when it is temporary *via* a decrease in protein translation. However, prolonged ISR without resolution can be harmful and lead to cell death, perhaps explaining, at least in part, the atrophy of the hippocampus and entorhinal cortex observed in FTD patients. These results underline the relevance of *Chchd10*$^{S59L/+}$ mice as a model for deciphering the mechanisms involved in the human disease.

Even though the exact role of neuroinflammation in neurodegeneration is still debated, it is a key component in both ALS and FTD. It has been proposed that neuroinflammation contributes to ISR activation, which can also sustain the inflammatory process through the overexpression of cytokines and NF-αB (for review see (Moon et al., 2018)). The proinflammatory cytokine TNF-α is required for eiF2α phosphorylation triggered by Aβ oligomers in AD disease models (Lourenco et al., 2013). Neuroinflammation affects various areas of the brain, in particular the hippocampal and parahippocampal regions. Collectively, our data show that *Chchd10*$^{S59L/+}$ mice present signs of neuroinflammation in the hippocampal and parahippocampal regions from the age of 5 months which are much more pronounced at 10 months of age, where the mice exhibit reduced synaptic plasticity and substantial decline in performance of an episodic memory task that depends on entorhinal cortical projections. From AD animal models, it is known that chronic neuroinflammation results in the loss of pyramidal cells within layers II and III of the entorhinal cortex and a significant attenuation of LTP within the dentate gyrus, leading to a temporal lobe atrophy, memory deficits and dementia (Janelsins et al., 2005); (Li et al., 2022).

Neuroinflammation in ALS/FTD is primarily characterized by reactive gliosis affecting both microglia and astrocytes in the CNS. The bulk of evidence from imaging studies in humans, and pathology studies in model organisms support that this process occurs early, long before neuronal cell death, *via* yet unknown signaling events between injured neurons and neighboring glial cells. We found evidence of gliosis, in the hippocampal and parahippocampal regions of the *Chchd10*$^{S59L/+}$ mice, characterized by the upregulation of astrocytic (GFAP), microglial (CD11b, CX3CR1) markers, glia proliferation and the secretion of proinflammatory cytokines (IL-1α, IL-6, TNF-α). Clear evidence of microglial and astrocytic activation has been found in SOD1, TDP43 and *C9orf72* models of ALS (for review see (Vahsen et al., 2021)). C9orf72 is required for the normal function of myeloid cells and altered microglial function, with increased expression of IL-6 and IL-1β and upregulation of inflammatory genes, may contribute to neurodegeneration in *C9orf72* expansion carriers (O'Rourke et al., 2016). SOD1 models indicate that microglial activation has neurotoxic effects. Most studies with SOD1, TDP43 and *C9orf72* models also support a neurotoxic astrocyte phenotype that could be mediated by crosstalk with other non-neuronal cells (Vahsen et al., 2021).

In conclusion, *Chchd10*$^{S59L/+}$ mice display pathological phenotypes associated with FTD in patients, including behavioral disorders suggestive of impaired learning and memory capacities.

Such results are consistent with the hippocampal lesions observed in these animals: ISR activation, protein aggregation, gliosis and neuronal degeneration. They demonstrate the value of *Chchd10*$^{S59L/+}$ mice, which recapitulate all the disorders found in patients expressing *CHCHD10*

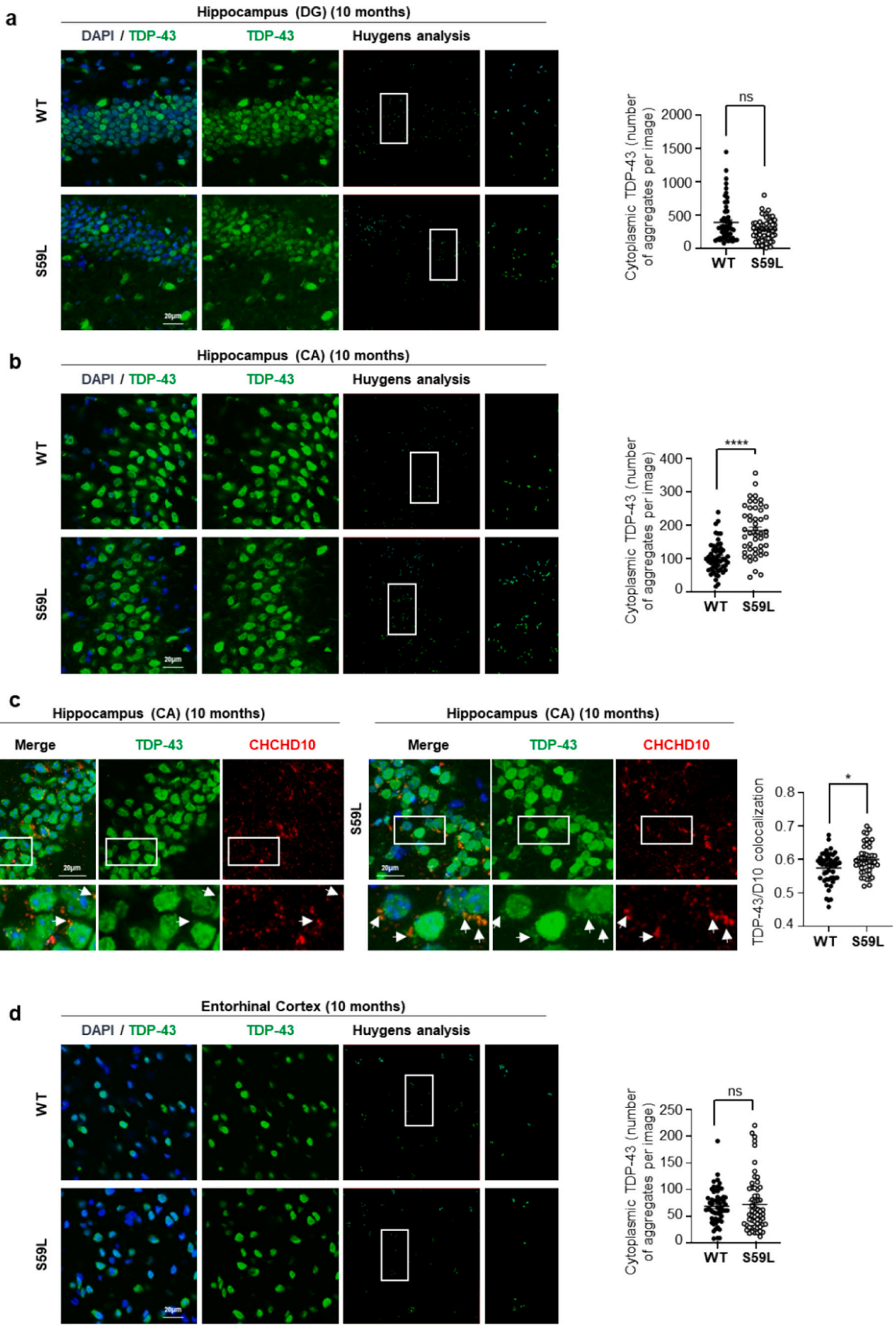

(caption on next page)

Fig. 6. Cytoplasmic TDP-43 inclusions and colocalization between TDP-43 and CHCHD10 in *Chchd10*$^{S59L/+}$ mice. a, No increase in cytoplasmic TDP-43 inclusions in the DG of the hippocampus of *Chchd10*$^{S59L/+}$ mice. Brain sections from *Chchd10*$^{S59L/+}$ mice (S59L/+) and control littermates (WT) at 10-month-old (left panel). Quantification of cytoplasmic TDP-43 inclusions (right panel). **b,** Accumulation of cytoplasmic TDP-43 inclusions in the CA of the hippocampus of *Chchd10*$^{S59L/+}$ mice. Brain sections of the CA from *Chchd10*$^{S59L/+}$ mice (S59L/+) and control littermates (WT) at 10-month-old (left panel). Quantification of cytoplasmic TDP-43 inclusions (right panel). **c,** TDP-43 and CHCHD10 in the same cytoplasmic inclusions (arrows) in the CA of the hippocampus of *Chchd10*$^{S59L/+}$ mice. Brain sections visualizing the CA from *Chchd10*$^{S59L/+}$ mice (S59L/+) and control littermates (WT) at 10-month-old (left panel). Quantification of colocalization between TDP-43 and CHCHD10 (D10) (right panel). **d,** No increase in cytoplasmic inclusions of TDP-43 in the entorhinal cortex of *Chchd10*$^{S59L/+}$ mice. Brain sections showing the entorhinal cortex from *Chchd10*$^{S59L/+}$ mice (S59L/+) and control littermates (WT) at 10-month-old (left panel). Quantification of cytoplasmic TDP-43 inclusions (right panel). **a-d,** Immunolabeling was performed with antibodies against TDP-43 (green) and/or CHCHD10 (red). DAPI was used for nuclear staining. Scale bar = 20 μm. n = 3 independent experiments with 3 *Chchd10*$^{S59L/+}$ mice and 3 control littermates. The data are represented as means ± SEM. P-value = * < 0.05, **** < 0.0001, ns = not significant. To quantify the number of cytoplasmic TDP-43 inclusions in **a**, **b** and **d**, analysis was performed using Huygens Essential Software™. (For interpretation of the references to colour in this figure legend, the reader is referred to the web version of this article.)

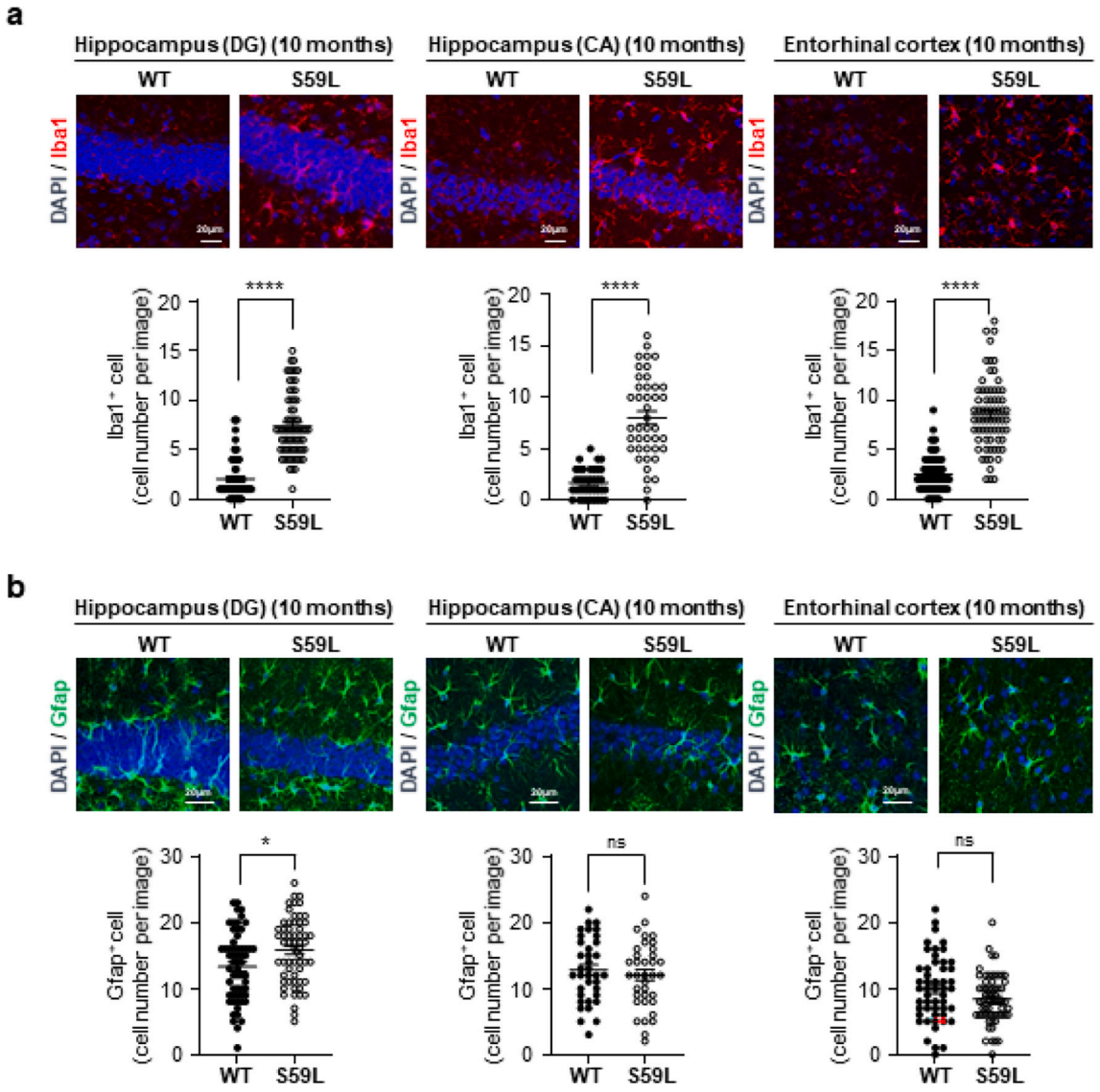

Fig. 7. Microglial proliferation in the hippocampus and the entorhinal cortex of Chchd*10*$^{S59L/+}$ mice. a-b, Brain sections visualizing hippocampal areas: DG and CA and the entorhinal cortex from *Chchd10*$^{S59L/+}$ mice (S59L/+) and control littermates (WT) at 10-month old (upper panels). Immunolabeling was performed with antibodies against Iba1 (red) (**a**) or GFAP (green) (**b**). DAPI was used for nuclear staining. Scale bar = 20 μm. Lower panels correspond to quantification of Iba1 or GFAP positive cells. Quantification of Iba1 (**a**) or GFAP (**b**) positive cells in DG (left panel) and CA (middle panel) and the entorhinal cortex (right panel) from 3 *Chchd10*$^{S59L/+}$ mice and 3 control littermates. The data are represented as means ± SEM. *P*-value = * < 0.05, **** < 0.0001, ns = not significant. (For interpretation of the references to colour in this figure legend, the reader is referred to the web version of this article.)

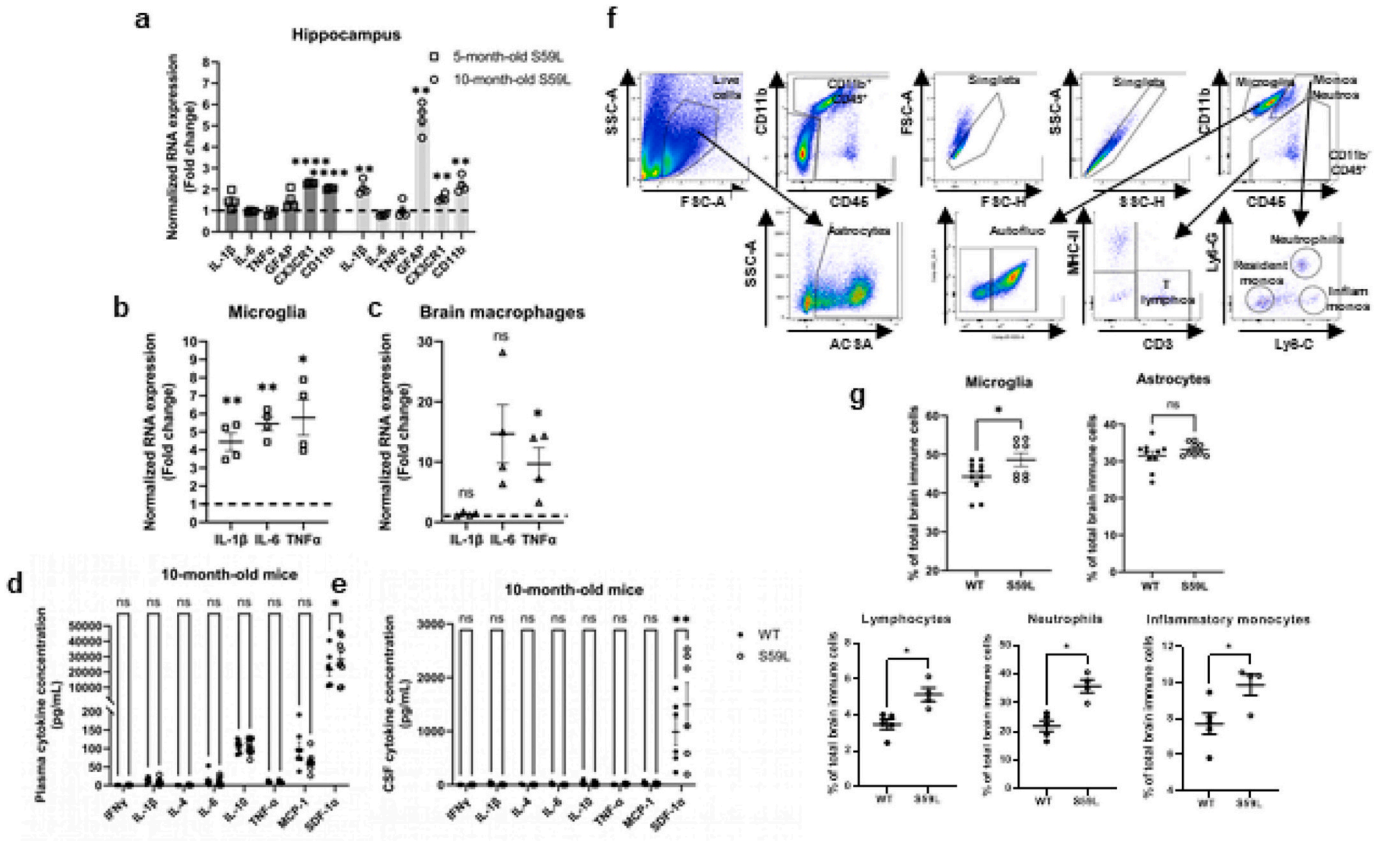

Fig. 8. mRNA and immune cell analyses reveal neuroinflammatory features in *Chchd10*$^{S59L/+}$ hippocampal region.
a Expression of inflammatory cytokines (IL-1β, IL-6 and TNFα) and glial genes (GFAP, CX3CR1 and CD11b) was measured by RT-qPCR in the hippocampus from 5- and 10-month-old WT and S59L mice. Bars represent the mean expression levels ± s (where $s = \sqrt{(s1^2 + s2^2)}$, s1 = standard deviation of the ΔCt of the gene of interest among replicates and s2 = standard deviation of the Ct of the housekeepping genes among replicates) expressed as fold change compared to age-related WT mouse hippocampus (dashed line). One sample *t*-test was performed on results, indicating gliosis reaction and inflammation in hippocampus of S59L mice. $^{**}p < 0.01$; $^{****}p < 0.001$. $N = 4$. **b, c,** Microglia (**b**) and brain-associated macrophages (**c**) were isolated by cell sorting from hippocampal and peri-hippocampal brain regions of 10-month-old WT and S59L mice. IL-1β, IL-6 and TNFα mRNA expression was measured by RT-qPCR. Bars represent the mean expression levels ± s expressed as fold change compared to age-related WT corresponding brain immune cells (dashed lines). One-sample t-test was performed on results. Results show that microglia isolated from 10-month-old S59L hippocampus region express significantly higher levels of IL-1β, IL-6 and TNFα mRNAs as compared to WT. Brain-associated macrophages isolated from 10-month-old S59L hippocampus region express higher level of TNFα mRNA. * $p < 0.05$; **p < 0.01; ns, non significant. $N = 4$. **d, e** Cytokine and chemokine levels were measured by immunoassay in plasma (**d**) and CSF (**e**) of 10-month-old WT (black dots) and S59L (white dots) mice. Results show that SDF-1α is significantly increased in both plasma and CSF from S59L mice as compared to WT. The data are represented as means ± SEM and analyzed using a two-way ANOVA followed by multiple comparison test. * p < 0.05; **p < 0.01; ns, non significant. $N = 6$. **f,** Representative bivariate dot plots of isolated brain cells illustrating gating strategy on live singlets ACSA$^+$ for astrocytes, CD11b$^+$/CD45^{low} for microglia, CD11b$^+$/CD45^{high}/Lys6-C$^-$/Lys6-G$^-$ for CNS-associated monocytes, CD11b$^+$/CD45^{high}/Lys6-C$^+$/Lys6-G$^-$ for brain-associated inflammatory monocytes, and CD11b$^+$/CD45^{high}/Lys6-C$^+$/Lys6-G^{med} for brain-associated neutrophils. **g,** Percentages of microglia, astrocytes, lymphocytes, neutrophils, and brain-associated inflammatory monocytes were determined in the total live brain immune cell suspension isolated from hippocampal and peri-hippocampal brain regions of 10-month-old WT (black dots) and S59L (white dots) mice. The data are represented as means ± SEM and analyzed using a Mann&Withney test. Results show an increase in the percentages of microglia, lymphocytes, neurotrophils and inflammatory monocytes in 10-month-old S59L hippocampus region as compared to WT animals. * p < 0.05; ns, non significant. $N = 4$.

variants. These KI mice represent a relevant model both for understanding the link between mitochondrial dysfunction and neurodegenerative diseases and for testing the preclinical efficacy of molecules with therapeutic aims.

Supplementary data to this article can be found online at https://doi.org/10.1016/j.nbd.2024.106498.

Ethics approval and consent to participate

Not applicable.

Consent for publication

Not applicable.

Funding

This work was made possible by grants to VP-F and AP-P from Investissements d'avenir UCA^{JEDI} n°ANR-15-IDEX-01.

CRediT authorship contribution statement

Emmanuelle C. Genin: Formal analysis, Conceptualization, Investigation, Methodology. **Pauline Pozzo di Borgo:** Data curation, Formal analysis. **Thomas Lorivel:** Formal analysis, Methodology. **Sandrine Hugues:** Data curation, Formal analysis, Methodology. **Mélissa Farinelli:** Data curation, Formal analysis, Methodology. **Alessandra Mauri-Crouzet:** Data curation. **Françoise Lespinasse:** Data curation. **Lucas Godin:** Data curation, Formal analysis. **Véronique Paquis-Flucklinger:** Conceptualization, Funding acquisition, Project administration, Supervision, Validation, Writing – original draft. **Agnès Petit-**

Paitel: Supervision, Validation, Writing – original draft, Conceptualization, Data curation, Formal analysis, Funding acquisition, Methodology, Project administration.

Declaration of competing interest

None.

Data availability

The datasets used and/or analyzed during the current study are available from the corresponding author on reasonable request.

Acknowledgements

We are grateful to the IRCAN's Molecular and Cellular Core Imaging facility, supported financially by FEDER, Conseil régional PACA, Conseil Départemental 06, Cancéropôle PACA, Gis Ibisa and Inserm, the IRCAN's Animal core facility, supported by FEDER, Région Provence Alpes-Côte d'Azur, Conseil Départemental 06 and Inserm and the IRCAN's Histology core facility, supported by Région PACA, Cancéropôle PACA, and Université Côte d'Azur. We wish to thank G. Lambeau for hosting part of the experiments, V.Thieffin and C. Carena for animal care at the IPMC's Animal core facility. The authors acknowledge the flow cytometry from the « Institut de Pharmacologie Moléculaire et Cellulaire » part of the « Microscopie Imagerie Cytométrie Azur» GIS IBiSA labeled platform as well as F. Aguila for graphic art work and Alice Guyon for careful proofreading.

References

Ahmed, R.M., Irish, M., van Eersel, J., Ittner, A., Ke, Y.D., Volkerling, A., van der Hoven, J., Tanaka, K., Karl, T., Kassiou, M., Kril, J.J., Piguet, O., Götz, J., Kiernan, M. C., Halliday, G.M., Hodges, J.R., Ittner, L.M., 2017 Mar. Mouse models of frontotemporal dementia: a comparison of phenotypes with clinical symptomatology. Neurosci. Biobehav. Rev. 74 (Pt A), 126–138. https://doi.org/10.1016/j.neubiorev.2017.01.004.

Ajroud-Driss, S., Fecto, F., Ajroud, K., et al., 2015. Mutation in the novel nuclear-encoded mitochondrial protein CHCHD10 in a family with autosomal dominant mitochondrial myopathy. Neurogenetics 16 (1), 1–9. https://doi.org/10.1007/s10048-014-0421-1.

Anderson, C.J., Bredvik, K., Burstein, S.R., Davis, C., Meadows, S.M., Dash, J., Case, L., Milner, T.A., Kawamata, H., Zuberi, A., Piersigilli, A., Lutz, C., Manfredi, G., 2019 Jul. ALS/FTD mutant CHCHD10 mice reveal a tissue-specific toxic gain-of-function and mitochondrial stress response. Acta Neuropathol. 138 (1), 103–121. https://doi.org/10.1007/s00401-019-01989-y.

Andrés-Benito, P., Povedano, M., Domínguez, R., Marco, C., Colomina, M.J., López-Pérez, Ó., Santana, I., Baldeiras, I., Martínez-Yelámos, S., Zerr, I., Llorens, F., Fernández-Irigoyen, J., Santamaría, E., Ferrer, I., 2020. Increased C-X-C motif chemokine ligand 12 levels in cerebrospinal fluid as a candidate biomarker in sporadic amyotrophic lateral sclerosis. Int. J. Mol. Sci. 21 (22), 8680. https://doi.org/10.3390/ijms21228680. Nov 17. PMID: 33213069; PMCID: PMC7698527.

Auranen, M., Ylikallio, E., Shcherbii, M., et al., 2015. CHCHD10 variant p.(Gly66Val) causes axonal Charcot- Marie-tooth disease. Neurol Genet. 1 (1), e1. Published 2015 Mar 26. doi:10.1212/NXG. 0000000000000003.

Bannwarth, S., Ait-El-Mkadem, S., Chaussenot, A., et al., 2014. A mitochondrial origin for frontotemporal dementia and amyotrophic lateral sclerosis through CHCHD10 involvement. Brain 137 (Pt 8), 2329–2345. https://doi.org/10.1093/brain/awu138.

Benussi, A., Premi, E., Gazzina, S., Brattini, C., Bonomi, E., Alberici, A., Jiskoot, L., van Swieten, J.C., Sanchez-Valle, R., Moreno, F., Laforce, R., Graff, C., Synofzik, M., Galimberti, D., Masellis, M., Tartaglia, C., Rowe, J.B., Finger, E., Vandenberghe, R., de Mendonça, A., Tagliavini, F., Santana, I., Ducharme, S., Butler, C.R., Gerhard, A., Levin, J., Danek, A., Otto, M., Frisoni, G., Ghidoni, R., Sorbi, S., Le Ber, I., Pasquier, F., Peakman, G., Todd, E., Bocchetta, M., Rohrer, J.D., Borroni, B., Genetic FTD Initiative (GENFI), 2021 Jan 4. Progression of Behavioral Disturbances and Neuropsychiatric Symptoms in Patients With Genetic Frontotemporal Dementia. JAMA Netw. Open 4 (1), e2030194. https://doi.org/10.1001/jamanetworkopen.2020.30194. Erratum in: JAMA Netw Open. 2021 Mar 1;4(3): e217664. PMID: 33404617; PMCID: PMC7788468.

Cazareth, J., Guyon, A., Heurteaux, C., Chabry, J., Petit-Paitel, A., 2014 Jul. Molecular and cellular neuroinflammatory status of mouse brain after systemic lipopolysaccharide challenge: importance of CCR2/CCL2 signaling. J. Neuroinflammation 28 (11), 132. https://doi.org/10.1186/1742-2094-11-132. PMID: 25065370; PMCID: PMC4237883.

Chaussenot, A., Le Ber, I., Ait-El-Mkadem, S., et al., 2014. Screening of CHCHD10 in a French cohort confirms the involvement of this gene in frontotemporal dementia with amyotrophic lateral sclerosis patients. Neurobiol. Aging 35 (12), 2884. e1–2884.e4. https://doi.org/10.1016/j.neurobiolaging.2014.07.022.

Chesnokova, E., Bal, N., Kolosov, P., 2017. Kinases of eIF2a switch translation of mRNA subset during neuronal plasticity. Int. J. Mol. Sci. 18 (10), 2213. https://doi.org/10.3390/ijms18102213. Oct 22. PMID: 29065505; PMCID: PMC5666893.

Clark, R.A., Shoaib, M., Hewitt, K.N., Stanford, S.C., Bate, S.T., 2012. A comparison of InVivoStat with other statistical software packages for analysis of data generated from animal experiments. J. Psychopharmacol. 26 (8), 1136–1142. https://doi.org/10.1177/0269881111420313. Aug. Epub 2011 Nov 8. PMID: 22071578.

Costa-Mattioli, M., Walter, P., 2020 Apr 24. The integrated stress response: From mechanism to disease. Science 368 (6489), eaat5314. https://doi.org/10.1126/science.aat5314. PMID: 32327570; PMCID: PMC8997189.

Costa-Mattioli, M., Gobert, D., Stern, E., Gamache, K., Colina, R., Cuello, C., Sossin, W., Kaufman, R., Pelletier, J., Rosenblum, K., Krnjević, K., Lacaille, J.C., Nader, K., Sonenberg, N., 2007. eIF2alpha phosphorylation bidirectionally regulates the switch from short- to long-term synaptic plasticity and memory. Cell 129 (1), 195–206. https://doi.org/10.1016/j.cell.2007.01.050. Apr 6. PMID: 17418795; PMCID: PMC4149214.

Fessler, E., Krumwiede, L., Jae, L.T., 2022. DELE1 tracks perturbed protein import and processing in human mitochondria. Nat. Commun. 13 (1), 1853. https://doi.org/10.1038/s41467-022-29479-y. Apr 6. PMID: 35388015; PMCID: PMC8986780.

Genin, E.C., Plutino, M., Bannwarth, S., Villa, E., Cisneros-Barroso, E., Roy, M., Ortega-Vila, B., Fragaki, K., Lespinasse, F., Pinero-Martos, E., Augé, G., Moore, D., Burté, F., Lacas-Gervais, S., Kageyama, Y., Itoh, K., Yu-Wai-Man, P., Sesaki, H., Ricci, J.E., Vives-Bauza, C., Paquis-Flucklinger, V., 2016. CHCHD10 mutations promote loss of mitochondrial cristae junctions with impaired mitochondrial genome maintenance and inhibition of apoptosis. EMBO Mol. Med. 8 (1), 58–72. https://doi.org/10.15252/emmm.201505496. Jan 1. PMID: 26666268; PMCID: PMC4718158.

Genin, E.C., Bannwarth, S., Lespinasse, F., Ortega-Vila, B., Fragaki, K., Itoh, K., Villa, E., Lacas-Gervais, S., Jokela, M., Auranen, M., Ylikallio, E., Mauri-Crouzet, A., Tyynismaa, H., Vihola, A., Augé, G., Cochaud, C., Sesaki, H., Ricci, J.E., Udd, B., Vives-Bauza, C., Paquis-Flucklinger, V., 2018. Loss of MICOS complex integrity and mitochondrial damage, but not TDP-43 mitochondrial localisation, are likely associated with severity of CHCHD10-related diseases. Neurobiol. Dis. 119, 159–171. https://doi.org/10.1016/j.nbd.2018.07.027. Nov. (Epub 2018 Aug 6. PMID: 30092269; PMCID: PMC7015038).

Genin, E.C., Madji Hounoum, B., Bannwarth, S., et al., 2019. Mitochondrial defect in muscle precedes neuromuscular junction degeneration and motor neuron death in CHCHD10S59L/+ mouse. Acta Neuropathol. 138 (1), 123–145. https://doi.org/10.1007/s00401-019-01988-z.

Genin, E.C., Bannwarth, S., Ropert, B., Lespinasse, F., Mauri-Crouzet, A., Augé, G., Fragaki, K., Cochaud, C., Donnarumma, E., Lacas-Gervais, S., Wai, T., Paquis-Flucklinger, V., 2022. CHCHD10 and SLP2 control the stability of the PHB complex: a key factor for motor neuron viability. Brain 145 (10), 3415–3430. https://doi.org/10.1093/brain/awac197. Oct 21. (PMID: 35656794).

Genin, E.C., Abou-Ali, M., Paquis-Flucklinger, V., 2023. Mitochondria, a key target in amyotrophic lateral sclerosis pathogenesis. Genes (Basel) 14 (11), 1981. https://doi.org/10.3390/genes14111981. Oct 24. PMID: 38002924; PMCID: PMC10671245.

Ittner, L.M., Fath, T., Ke, Y.D., Bi, M., van Eersel, J., Li, K.M., Gunning, P., Götz, J., 2008. Parkinsonism and impaired axonal transport in a mouse model of frontotemporal dementia. Proc. Natl. Acad. Sci. USA 105 (41), 15997–16002. https://doi.org/10.1073/pnas.0808084105. Oct 14.

Janelsins, M.C., Mastrangelo, M.A., Oddo, S., LaFerla, F.M., Federoff, H.J., Bowers, W.J., 2005. Early correlation of microglial activation with enhanced tumor necrosis factor-alpha and monocyte chemoattractant protein-1 expression specifically within the entorhinal cortex of triple transgenic Alzheimer's disease mice. J. Neuroinflammation 18 (2), 23. https://doi.org/10.1186/1742-2094-2-23. Oct. PMID: 16232318; PMCID: PMC1276812.

Johnson, J.O., Glynn, S.M., Gibbs, J.R., et al., 2014. Mutations in the CHCHD10 gene are a common cause of familial amyotrophic lateral sclerosis. Brain 137 (Pt 12), e311. https://doi.org/10.1093/brain/awu265.

Li, M.L., Wu, S.H., Song, B., Yang, J., Fan, L.Y., Yang, Y., Wang, Y.C., Yang, J.H., Xu, Y., 2022 Nov. Single-cell analysis reveals transcriptomic reprogramming in aging primate entorhinal cortex and the relevance with Alzheimer's disease. Aging Cell 21 (11), e13723. https://doi.org/10.1111/acel.13723. Epub 2022 Sep 27. PMID: 36165462; PMCID: PMC9649611.

Liu, T., Woo, J.A., Bukhari, M.Z., Wang, X., Yan, Y., Buosi, S.C., Ermekbaeva, A., Sista, A., Kotsiviras, P., LePochat, P., Chacko, A., Zhao, X., Kang, D.E., 2022. Modulation of synaptic plasticity, motor unit physiology, and TDP-43 pathology by CHCHD10. Acta Neuropathol. Commun. 10 (1), 95. https://doi.org/10.1186/s40478-022-01386-9. Jul 4. PMID: 35787294; PMCID: PMC9254494.

Lourenco, M.V., Clarke, J.R., Frozza, R.L., Bomfim, T.R., Forny-Germano, L., Batista, A. F., Sathler, L.B., Brito-Moreira, J., Amaral, O.B., Silva, C.A., Freitas-Correa, L., Espírito-Santo, S., Campello-Costa, P., Houzel, J.C., Klein, W.L., Holscher, C., Carvalheira, J.B., Silva, A.M., Velloso, L.A., Munoz, D.P., Ferreira, S.T., De Felice, F. G., 2013. TNF-α mediates PKR-dependent memory impairment and brain IRS-1 inhibition induced by Alzheimer's β-amyloid oligomers in mice and monkeys. Cell Metab. 18 (6), 831–843. https://doi.org/10.1016/j.cmet.2013.11.002. Dec 3. (PMID: 24315369).

Mitsopoulos, P., Chang, Y.H., Wai, T., et al., 2015. Stomatin-like protein 2 is required for in vivo mitochondrial respiratory chain supercom- plex formation and optimal cell function. Mol. Cell. Biol. 35, 1838–1847.

Moon, S.L., Sonenberg, N., Parker, R., 2018. Neuronal regulation of eIF2α function in health and neurological disorders. Trends Mol. Med. 24 (6), 575–589. https://doi.org/10.1016/j.molmed.2018.04.001. Jun. Epub 2018 Apr 30. PMID: 29716790.

Müller, K., Andersen, P.M., Hübers, A., et al., 2014. Two novel mutations in conserved codons indicate that CHCHD10 is a gene associated with motor neuron disease. Brain 137 (Pt 12), e309. https://doi.org/10.1093/brain /awu227.

O'Rourke, J.G., Bogdanik, L., Yáñez, A., Lall, D., Wolf, A.J., Muhammad, A.K., Ho, R., Carmona, S., Vit, J.P., Zarrow, J., Kim, K.J., Bell, S., Harms, M.B., Miller, T.M., Dangler, C.A., Underhill, D.M., Goodridge, H.S., Lutz, C.M., Baloh, R.H., 2016. C9orf72 is required for proper macrophage and microglial function in mice. Science 351 (6279), 1324–1329. https://doi.org/10.1126/science.aaf1064. Mar 18. PMID: 26989253; PMCID: PMC5120541.

Parobkova, E., Matej, R., 2021. Amyotrophic lateral sclerosis and frontotemporal lobar degenerations: similarities in genetic background. Diagnostics (Basel). 11 (3), 509. https://doi.org/10.3390/diagnostics11030509. Mar 13. PMID: 33805659; PMCID: PMC7998502.

Penttilä, S., Jokela, M., Bouquin, H., Saukkonen, A.M., Toivanen, J., Udd, B., 2015. Late onset spinal motor neuronopathy is caused by mutation in CHCHD10. Ann. Neurol. 77 (1), 163–172. https://doi.org/10.1002/ana. 24319.

Ratnavalli, E., Brayne, C., Dawson, K., Hodges, J.R., 2002. The prevalence of frontotemporal dementia. Neurology 58 (11), 1615–1621. https://doi.org/10.1212/wnl.58.11.1615. Jun 11.

Shammas, M.K., Huang, X., Wu, B.P., Fessler, E., Song, I.Y., Randolph, N.P., Li, Y., Bleck, C.K., Springer, D.A., Fratter, C., Barbosa, I.A., Powers, A.F., Quirós, P.M., Lopez-Otin, C., Jae, L.T., Poulton, J., Narendra, D.P., 2022. OMA1 mediates local and global stress responses against protein misfolding in CHCHD10 mitochondrial myopathy. J. Clin. Invest. 132 (14), e157504. https://doi.org/10.1172/JCI157504. Jul 15.

Signorile, A., Sgaramella, G., Bellomo, F., De Rasmo, D., 2019. Prohibitins: a critical role in mitochondrial functions and implication in diseases. Cells 8, 71.

Sik, A., van Nieuwehuyzen, P., Prickaerts, J., Blokland, A., 2003. Performance of different mouse strains in an object recognition task. Behav. Brain Res. 147 (1–2), 49–54. https://doi.org/10.1016/s0166-4328(03)00117-7. Dec 17. (PMID: 14659569).

Sirkis, D.W., Geier, E.G., Bonham, L.W., Karch, C.M., Yokoyama, J.S., 2019. Recent advances in the genetics of frontotemporal dementia. Curr. Genet. Med. Rep. 7 (1), 41–52. https://doi.org/10.1007/s40142-019-0160-6.

Snowden, J.S., 2023. Changing perspectives on frontotemporal dementia: a review. J. Neuropsychol. 17 (2), 211–234. https://doi.org/10.1111/jnp.12297. Jun. Epub 2022 Oct 31. PMID: 36315040.

Steglich, G., Neupert, W., Langer, T., 1999. Prohibitins regulate membrane protein degradation by the m-AAA protease in mitochondria. Mol. Cell. Biol. 19 (5), 3435–3442. https://doi.org/10.1128/MCB.19.5.3435. May. PMID: 10207067; PMCID: PMC84136.

Trinh, M.A., Klann, E., 2013 Oct. Translational control by eIF2α kinases in long-lasting synaptic plasticity and long-term memory. Neurobiol. Learn. Mem. 105 https://doi.org/10.1016/j.nlm.2013.04.013, 93–9. Epub 2013 May 22. PMID: 23707798; PMCID: PMC3769507.

Tsai, K.J., Yang, C.H., Fang, Y.H., Cho, K.H., Chien, W.L., Wang, W.T., Wu, T.W., Lin, C. P., Fu, W.M., Shen, C.K., 2010. Elevated expression of TDP-43 in the forebrain of mice is sufficient to cause neurological and pathological phenotypes mimicking FTLD-U. J. Exp. Med. 207 (8), 1661–1673. https://doi.org/10.1084/jem.20092164. Aug 2.

Vahsen, B.F., Gray, E., Thompson, A.G., Ansorge, O., Anthony, D.C., Cowley, S.A., Talbot, K., Turner, M.R., 2021. Non-neuronal cells in amyotrophic lateral sclerosis - from pathogenesis to biomarkers. Nat. Rev. Neurol. 17 (6), 333–348. https://doi.org/10.1038/s41582-021-00487-8. Jun. Epub 2021 Apr 29. PMID: 33927394.

Wai, T., Saita, S., Nolte, H., Müller, S., König, T., Richter-Dennerlein, R., Sprenger, H.G., Madrenas, J., Mühlmeister, M., Brandt, U., Krüger, M., Langer, T., 2016 Dec. The membrane scaffold SLP2 anchors a proteolytic hub in mitochondria containing PARL and the i-AAA protease YME1L. EMBO Rep. 17 (12), 1844–1856. https://doi.org/10.15252/embr.201642698. Epub 2016 Oct 13. PMID: 27737933; PMCID: PMC5283581.